Monthly Notices of the ROYAL ASTRONOMICAL SOCIETY

MNRAS **499,** 362–378 (2020) doi:10.1093/mnras/staa2718
Advance Access publication 2020 September 7

Observational signatures of disc and jet misalignment in images of accreting black holes

K. Chatterjee [1]★ Z. Younsi,[2,3] M. Liska,[1,4]† A. Tchekhovskoy,[5] S. B. Markoff [1,6] D. Yoon [1] D. van Eijnatten,[1] C. Hesp [1] A. Ingram [7] and M. B. M. van der Klis[1]

[1]*Anton Pannekoek Institute for Astronomy, University of Amsterdam, Science Park 904, NL-1098 XH Amsterdam, the Netherlands*
[2]*Mullard Space Science Laboratory, University College London, Holmbury St. Mary, Dorking, Surrey RH5 6NT, UK*
[3]*Institut für Theoretische Physik, Goethe-Universität Frankfurt, Max-von-Laue-Straße 1, D-60438 Frankfurt am Main, Germany*
[4]*Institute for Theory and Computation, Harvard University, 60 Garden Street, Cambridge, MA 02138, USA*
[5]*Center for Interdisciplinary Exploration & Research in Astrophysics (CIERA), Physics & Astronomy, Northwestern University, Evanston, IL 60202, USA*
[6]*Gravitation Astroparticle Physics Amsterdam (GRAPPA) Institute, University of Amsterdam, Science Park 904, NL-1098 XH Amsterdam, the Netherlands*
[7]*Astrophysics, Department of Physics, University of Oxford, Denys Wilkinson Building, Keble Road, Oxford OX1 3RH, UK*

Accepted 2020 September 1. Received 2020 August 30; in original form 2020 February 19

ABSTRACT

Black hole (BH) accretion is one of nature's most efficient energy extraction processes. When gas falls in, a significant fraction of its gravitational binding energy is either converted into radiation or flows outwards in the form of BH-driven jets and disc-driven winds. Recently, the Event Horizon Telescope (EHT), an Earth-sized submillimetre radio interferometer, captured the first images of M87's BH. These images were analysed and interpreted using general relativistic magnetohydrodynamics (GRMHD) models of accretion discs with rotation axes aligned with the BH spin axis. However, since infalling gas is often insensitive to the BH spin direction, misalignment between accretion disc and BH spin may be a common occurrence in nature. In this work, we use the general relativistic radiative transfer code BHOSS to calculate the first synthetic radio images of (highly) tilted disc/jet models generated by our GPU-accelerated GRMHD code H-AMR . While the tilt does not have a noticeable effect on the system dynamics beyond a few tens of gravitational radii from the BH, the warping of the disc and jet can imprint observable signatures in EHT images on smaller scales. Comparing the images from our GRMHD models to the 43 and 230 GHz EHT images of M87, we find that M87 may feature a tilted disc/jet system. Further, tilted discs and jets display significant time variability in the 230 GHz flux that can be further tested by longer-duration EHT observations of M87.

Key words: accretion, accretion discs – black hole physics – MHD – methods: numerical – galaxies: active – galaxies: jets.

1 INTRODUCTION

There is observational evidence for misalignment between the accretion disc and black hole (BH) spin axis in both active galactic nuclei (AGNs) and BH X-ray binaries (XRBs; e.g. Hjellming & Rupen 1995; Greene, Bailyn & Orosz 2001; Maccarone 2002; Caproni et al. 2006; van den Eijnden et al. 2017; Russell et al. 2019), and tidal disruption events (e.g. Pasham et al. 2019), with theoretical studies of the growth of supermassive black holes (SMBHs) favouring randomly oriented accretion and affecting BH spin evolution (e.g. Volonteri et al. 2005; King & Pringle 2006). In particular, periodic variations in the jet position with respect to the line of sight have been invoked for explaining quasi-periodic oscillations (QPOs) in the emission of some sources (e.g. Stella & Vietri 1998; Ingram, Done & Fragile 2009). The rotational plane of BH accretion discs is therefore expected to be misaligned with respect to the BH spin axis, as infalling gas from large distances will typically not be sensitive to the direction of rotation of the central BH. However, there is still much uncertainty over this claim; but, with recent advancements in very long baseline interferometry (VLBI) techniques, most notably the Event Horizon Telescope (EHT; Doeleman et al. 2008; EHTC 2019a), as well as growing interest in space VLBI (e.g. Palumbo et al. 2019; Roelofs et al. 2019; Fish, Shea & Akiyama 2020), imaging the near-horizon region (i.e. $r \lesssim 20\ r_{\rm g}$, where $r_{\rm g} \equiv GM/c^2$ is the gravitational radius of the BH, M is its mass, G is the gravitational constant, and c is the speed of light) for SMBHs has become a reality, making it possible to directly test for misalignment in Sagittarius A* (Sgr A*) and M87. In fact, Park et al. (2019) briefly discussed possible misalignment in M87.

Misalignment brings about important changes in the dynamics of the system via general relativistic (GR) frame dragging, which induces nodal Lense–Thirring precession (LT; Lense & Thirring 1918) of test particles on tilted orbits around the central object, with a radially dependent angular frequency $\Omega_{\rm LT} \propto 1/r^3$. Growing interest in the physics of accretion under the effects of LT precession led to modelling tilted accretion discs via general relativistic magnetohydrodynamics (GRMHD) simulations of both thick (e.g. Fragile & Anninos 2005; Fragile et al. 2007; McKinney, Tchekhovskoy & Blandford 2013; Polko & McKinney 2017; Liska et al. 2018; White,

★ E-mail: k.chatterjee@uva.nl
† John Harvard Distinguished Science and ITC Fellow.

Quataert & Blaes 2019) and thin (e.g. Liska et al. 2019b) tilted discs, some of which carry promising indications for the origin of specific kinds of QPOs (e.g. Liska et al. 2020). Of course, the absence of QPOs due to disc precession does not rule out misalignment, since tilted geometrically thick discs tend to have extremely long precession periods, resulting in quasi-stationary disc warps. Due to GR warping of the disc via pressure waves (Papaloizou & Lin 1995; Ivanov & Illarionov 1997; Lubow & Ogilvie 2000), Dexter & Fragile (2011) showed, via general relativistic radiative transfer (GRRT) of GRMHD simulations, that tilting the disc brings about significant changes in the appearance of the inner 20 $r_{\rm g}$ around a BH, e.g. when scaled to the mass and distance of Sgr A* (Dexter & Fragile 2013). GRMHD simulations found that tilted discs accrete on to the BH via two high-density plunging streams of infalling material (e.g. Fragile & Blaes 2008; Liska et al. 2018). Further, it has been shown that the narrow and highly warped morphology of these plunging streams can lead to the accumulation of gas near the point of highest disc tilt, developing a pair of standing shocks (Fragile & Blaes 2008; Generozov et al. 2013; White et al. 2019). Consequently, higher inflow temperatures resulting from shock heating dominate the emission (e.g. Dexter & Fragile 2013; White et al. 2020).

The magnetic field strength plays a vital role in a tilted disc system because magnetic fields provide an extra torque to the GR warping, and hence help in aligning the disc. In particular, Liska et al. (2018) found that for tilted precessing thick discs, the higher the disc magnetic field strength, the stronger the jets are and the more they tend to push the inner parts of the disc to align more closely with the BH spin axis. This can be understood because when the magnetic flux on to the BH is large enough to hinder accretion from the disc (Narayan, Igumenshchev & Abramowicz 2003), known as the magnetically arrested disc (MAD) condition, the associated jet efficiently extracts the BH's rotational energy (Tchekhovskoy & McKinney 2012) and becomes powerful enough to force the inner part of the disc to align with the BH spin axis (McKinney et al. 2013), while the large-scale jet remains aligned with the disc. Further, it was shown that in the absence of magnetic fields, the disc alignment is much weaker as compared to the MHD case (Sorathia, Krolik & Hawley 2013). Strongly magnetized jets can dictate dynamics along with jet–disc interactions, potentially developing shocks similar in nature to the pair of standing shocks present in the plunging streams. Misalignment can therefore introduce potential degeneracies in observed images and spectra, warranting further exploration so that we are able to more clearly interpret current and future EHT horizon-scale images. However, to date, images illustrating the warping of misaligned disc/jet systems (see also White et al. 2020 for misaligned disc images) and corresponding observational indications of tilt in spectra have not been studied and compared to observed images (e.g. EHTC 2019b).

In this work, we explore, for the first time, a variety of initial misalignment angles for a BH disc/jet system in high resolution using our GPU-accelerated GRMHD code H-AMR (Liska et al. 2019a). We further calculate observable images using the GRRT code BHOSS (Younsi et al. 2016, 2020). In Section 2, we give an overview of our methodology and simulation set-up. We present our results in Section 3. In Section 4, we compare our images to the recently published EHT image of M87 (EHTC 2019a). We conclude in Section 5.

2 METHODOLOGY AND NUMERICAL SET-UP

We use our state-of-the-art massively parallel, GPU-accelerated 3D GRMHD code H-AMR (Liska et al. 2018, 2019a; Chatterjee et al. 2019) to solve the GRMHD equations in a fixed Kerr space–time.

Table 1. Top: Parameters common to all models used in this work: dimensionless BH spin (a), simulation grid resolution, disc inner radius $r_{\rm in}$, disc pressure maximum radius $r_{\rm max}$, and outer grid radius $r_{\rm out}$. Bottom: model names, initial disc misalignment, density-weighted volume-averaged MRI quality factors $Q_{r,\theta,\varphi}$ (see text for definition), dimensionless horizon magnetic flux $\phi_{\rm BH}$ (equation 4), jet tilt $\mathcal{T}_{\rm j}$ and precession $\mathcal{P}_{\rm j}$ angles spatially averaged over [50, 150] $r_{\rm g}$, and total simulation time $t_{\rm sim}$. Quantities marked with * are time-averaged over [99 960, 100 960] $t_{\rm g}$, where $t_{\rm g} \equiv r_{\rm g}/c$.

Model	a	Resolution ($N_{\rm r} \times N_\theta \times N_\varphi$)	$r_{\rm in}$ ($r_{\rm g}$)	$r_{\rm max}$ ($r_{\rm g}$)	$r_{\rm out}$ ($r_{\rm g}$)
All	0.9375	448 × 144 × 240	12.5	25	10^5
Model	$\mathcal{T}_{\rm init}$ (deg)	Q-factor* (Q_r, Q_θ, Q_φ)	$\phi^*_{\rm BH}$	$\mathcal{T}^*_{\rm j}$, $\mathcal{P}^*_{\rm j}$ (deg, deg)	$t_{\rm sim}$ ($10^5 t_{\rm g}$)
T0	0	(18, 14, 99)	52.8	0.8, –	1.32
T30	30	(18, 26, 78)	45	22.7, 28.4	1.19
T60	60	(13, 28, 45)	27.8	43.4, 42.2	1.48

The H-AMR section in Porth et al. (2019) presents a description of the code attributes, such as adaptive mesh refinement (AMR), local adaptive time-stepping, and a staggered mesh for the magnetic field evolution, as well as comparisons to benchmark results for a standard accretion disc problem. We adopt the geometrical unit convention, $G = c = 1$, and further normalize the BH mass to $M = 1$, thereby normalizing the length-scale to the gravitational radius $r_{\rm g}$. We carry out the simulations in logarithmic Kerr–Schild coordinates with a numerical resolution $N_r \times N_\theta \times N_\varphi$ of 448 × 144 × 240 (Table 1), sufficient to resolve the magnetorotational instability (MRI; Balbus & Hawley 1991) in the disc. Our grid is axisymmetric and uniform in $\log(r/r_{\rm g})$, extending from 0.75 $r_{\rm hor}$ to 10^5 $r_{\rm g}$, where the event horizon radius $r_{\rm hor} \equiv r_{\rm g}(1 + \sqrt{1 - a^2})$, with $a = 0.9375$. A further description of the grid is given in Liska et al. (2018). We use outflowing boundary conditions (BCs) at the inner and outer r boundaries; transmissive polar BCs in the θ-direction and periodic BCs in the φ-direction. To quantify the MRI resolution, we calculate the quality factors $Q_{r,\theta,\varphi}$, where $Q_i = \langle 2\pi v^i_{\rm A} \rangle_w / \langle \Delta^i \Omega \rangle_w$ measures the number of cells per MRI wavelength in direction $i = [r, \theta, \varphi]$, volume-averaged over the disc ($r < 150\ r_{\rm g}$) with weight $w = \rho$, the gas density (see equations 18–20 in Liska et al. 2019b). Here, $v^i_{\rm A}$ is the Alfvén velocity, Δ^i the cell size, and Ω the angular velocity of the fluid. We achieve $Q_\theta \gtrsim 10$ (Table 1) during our chosen time period, fulfiling the numerical convergence criteria (see e.g. Hawley, Guan & Krolik 2011).

In all models, we start with a standard Fishbone & Moncrief (1976) torus in hydrostatic equilibrium around the central (spinning) Kerr BH. The torus inner edge is located at $r_{\rm in} = 12.5\ r_{\rm g}$ and the gas pressure ($p_{\rm g}$) maximum is at $r_{\rm max} = 25\ r_{\rm g}$, with the ideal gas law adiabatic index set to $\Gamma = 5/3$ (i.e. non-relativistic). The non-zero magnetic field vector potential is given by $A_\varphi \propto (\rho - 0.05)^2 (r/r_{\rm g})^3$ and normalized to $\max(p_{\rm g})/\max(p_{\rm B}) = 100$, where $p_{\rm g} \equiv (\Gamma - 1) u_{\rm g}$ is the gas pressure, $p_{\rm B} \equiv b^2/2$ is the magnetic pressure, and $u_{\rm g}$ is the fluid internal energy. Furthermore, the magnetic field 4-vector, b^μ, is defined in Lorentz–Heaviside units where a factor of $1/\sqrt{4\pi}$ is absorbed into its definition. Note that our model parameters are slightly different from the tilted disc models used in Fragile et al. (2007), where the authors use $r_{\rm in} = 15\ r_{\rm g}$ and $r_{\rm max} = 25\ r_{\rm g}$, an adiabatic index of $\Gamma = 5/3$, and vector potential $A_\varphi \propto \rho$, resulting in a smaller magnetic flux content in the torus. We also note that White et al. (2019) use similar parameters to Fragile et al. (2007), but with $\Gamma = 4/3$. We tilt our discs at three different angles: $\mathcal{T}_{\rm init} = 0°$ (model T0), 30°

(model T30; previously reported as model 'S25A93' in Liska et al. 2018), and 60° (model T60) with respect to the plane perpendicular to the BH spin axis (see Table 1). GRMHD simulations suffer from numerical errors in the jet funnel as pockets of low-density gas are created when matter either falls inwards due to the BH's gravity or is expelled outwards via magnetic forces, leading to truncation errors in the solution. In our simulations, we replenish the near-vacuum regions by ad hoc mass loading the jet funnel in the drift frame of the magnetic field by following Ressler et al. (2017) and further employ a floor model with $\rho c^2 \geq \max[p_{\rm B}/50,\ 2\times10^{-6}c^2(r/r_{\rm g})^{-2}]$ and $u_{\rm g} \geq \max[p_{\rm B}/150,\ 10^{-7}c^2(r/r_{\rm g})^{-2\Gamma}]$.

In order to capture the radiation output from our GRMHD simulations and calculate synthetic radio frequency images which are comparable with observational data, we perform GRRT calculations in post-processing using BHOSS: by ray tracing the GRMHD data and integrating the GRRT equations, the spectral properties of the emergent light produced in the strong gravitational field around the BH are calculated. The geodesic equations themselves are integrated backwards (from observer-to-source) using a fifth-order adaptive time-step Runge–Kutta–Fehlberg scheme (to maintain computational speed and accuracy), and the GRRT equations are integrated in tandem, using the reverse-integration approach introduced in Younsi, Wu & Fuerst (2012), including all emission, absorption, and optical depth effects of the plasma.

We set the camera latitude θ_0 (otherwise known as the observer inclination angle) and longitude φ_0 at a distance of 1000 $r_{\rm g}$ from the BH. The radiative transfer requires the BH mass and the mass accretion rate to set the physical scales of the simulation. We choose our target central BH to be that of the galaxy M87, dubbed 'M87∗', with a mass $M = 6.5\times10^9\ {\rm M}_\odot$ at a distance $D = 16.8$ Mpc (EHTC 2019c). For the rest of the text, we only use 'M87' when referring to the BH and jet properties. In this work, we consider a relativistic thermal Maxwell–Jüttner electron distribution function for the synchrotron absorption and emission (given by Leung, Gammie & Noble 2011), with the ion–electron temperature ratio set according to the Mościbrodzka, Falcke & Shiokawa (2016) prescription, namely

$$T_{\rm i}/T_{\rm e} := \frac{R_\ell + \beta_{\rm p}^2 R_{\rm h}}{1+\beta_{\rm p}^2}, \tag{1}$$

where $\beta_{\rm p} \equiv p_{\rm g}/p_{\rm B}$ is the plasma-β parameter, and $T_{\rm i}$ and $T_{\rm e}$ are the ion and electron temperatures, in Kelvin, respectively. This assumption for the electron temperature model is the same as used in EHTC (2019b). The dimensionless electron temperature is defined as

$$\Theta_{\rm e} := \frac{p_{\rm g}}{\rho}\frac{m_{\rm p}/m_{\rm e}}{T_{\rm i}/T_{\rm e}}, \tag{2}$$

where $m_{\rm p}$ and $m_{\rm e}$ are the proton and electron masses, respectively. The electron temperature in c.g.s. units is therefore simply $T_{\rm e} = m_{\rm e}c^2\Theta_{\rm e}/k_{\rm B}$, where $k_{\rm B}$ is the Boltzmann constant. In practice, equation (1) sets the temperature ratio in the jet ($\beta_{\rm p} \ll 1$) to be $T_{\rm i}/T_{\rm e} \sim R_\ell$ and in the disc ($\beta_{\rm p} \gg 1$), $T_{\rm i}/T_{\rm e} \sim R_{\rm h}$. For our models, we fix $R_\ell = 1$, while we vary $R_{\rm h} = (1, 10, 100)$. Additionally, we exclude all emission from the jet spine (defined where $b^2/\rho c^2 \geq 1$, where b is the fluid-frame magnetic field strength) as the gas density and temperature in this region may be affected by the simulation floors and are therefore unreliable.

3 RESULTS

Fig. 1 shows the gas density ρ, the plasma-β ($\beta_{\rm p}$), and the ion temperature $T_{\rm i}$ (in Kelvin) of the simulations at $t = 10^5\ t_{\rm g}$, clearly illustrating the misalignment of both the high-density disc and the low-density jet with respect to the BH spin direction, which points upwards in this figure. Each BH system is shown in the plane of the BH spin and the jet angular momentum vector, or, in other words, the $\varphi = 0°$ plane rotated by the corresponding jet precession angle $\mathcal{P}_{\rm j}$ (see Table 1). Fig. 1 also delineates the jet funnel (dark blue in the figure), given by $b^2/\rho c^2 = 1$ (red line) and the unbound material given by the Bernoulli parameter $Be := -hu_t = 1.02$ (black line), with the latter being taken as a proxy for the disc–wind region (light blue–green region). In the definition of Be, h and u_t are the enthalpy and the temporal component of the covariant velocity (interpreted as the conserved particle energy), respectively. Over time, in all three models the accretion disc develops turbulence via the MRI, leading to gas accretion on to the BH (Fig. 2a) in the form of plunging streams (Fragile et al. 2007; Liska et al. 2018). Figs 2(b) and (c) show that our chosen initial field configuration evolves to create a near-MAD disc in each case, with the dimensionless magnetic flux through the horizon $\phi_{\rm BH} = \Phi_{\rm BH}/(\langle\dot{M}\rangle r_{\rm g}c^2)^{1/2} \lesssim \phi_{\rm max} \approx 50$ (Tchekhovskoy, Narayan & McKinney 2011), producing highly efficient jets with $P_{\rm outflow}/(\langle\dot{M}\rangle c^2) \sim 1$, powered by BH rotational energy extracted via the Blandford–Znajek mechanism (Blandford & Znajek 1977). Here, we make use of the following definitions. The BH accretion rate (positive for inflow of gas towards the BH):

$$\dot{M} := -\iint \rho u^r\, {\rm d}A_{\theta\varphi}, \tag{3}$$

the magnetic flux at the event horizon:

$$\Phi_{\rm BH} := \frac{1}{2}\iint |B^r|\, {\rm d}A_{\theta\varphi}, \tag{4}$$

and the outflow power:

$$P_{\rm outflow} := \dot{M}c^2 - \dot{E}, \tag{5}$$

where the energy accretion rate is defined as $\dot{E} = \int\int T_t^r\, {\rm d}A_{\theta\varphi}$ (taken to be positive for inflow of energy towards the BH), u^r and B^r are the radial velocity and magnetic field, respectively, T_t^r is the total radial energy flux, ${\rm d}A_{\theta\varphi} = \sqrt{-g}\,{\rm d}\theta\,{\rm d}\varphi$ is the surface area element, and $g \equiv |g_{\mu\nu}|$ is the metric determinant.

Figs 2(d) and (e) show the disc/jet tilt and precession angles, spatially averaged over [50, 150] $r_{\rm g}$, and demonstrate that the large-scale jet is perpendicular to the large-scale disc on average (in agreement with Liska et al. 2018), with some oscillatory behaviour of the jet tilt and precession angles illustrating the jet's dynamic nature. Over time, the inner part of the misaligned discs tends to align with the plane perpendicular to the BH spin axis, with the tilt angle decreasing by roughly 25 per cent compared to the initial tilt. Further, even though we started with a compact disc, subsequent disc evolution causes the disc to puff up due to viscous spreading, as illustrated by the disc barycentric radius (Fig. 2f; see also Porth et al. 2019), given by

$$r_{\rm disc} = \frac{\int\int r\,\rho\,{\rm d}A_{\theta\varphi}}{\int\int \rho\,{\rm d}A_{\theta\varphi}}. \tag{6}$$

As the disc becomes substantially larger, it stops precessing and the disc and jet tilt angle become roughly constant at $t \gtrsim 9\times10^4\ t_{\rm g}$. Note that even though the disc and the jet no longer precess, they remain misaligned with respect to the BH spin vector, clearly illustrating that the absence of QPOs or any indication of precession does not rule out the presence of misalignment. Effectively, we end up with three disc/jet models with time- and spatially averaged jet tilt and precession angles $\{\mathcal{T}_{\rm j}, \mathcal{P}_{\rm j}\}$ as follows: T0: $\{0.8°, 0°\}$, T30: $\{22.7°, 28.4°\}$, and T60: $\{43.4°, 42.2°\}$ (see Table 1).

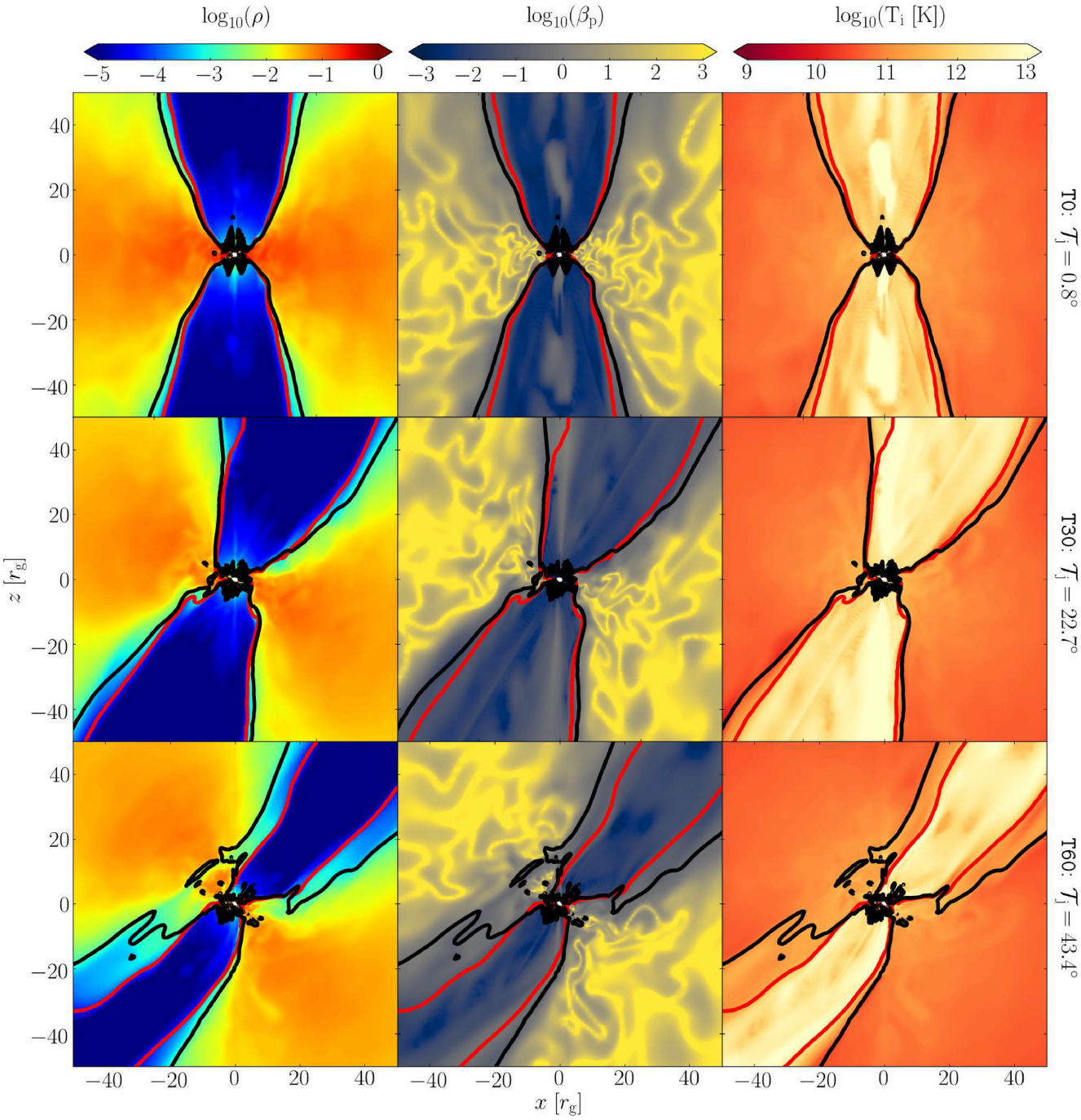

Figure 1. We show the 2D cross-sectional plots of the gas density and plasma-β in code units, and the ion temperature T_i (in Kelvin) for each tilt model: `T0`, `T30`, and `T60`, spanning 100 r_g × 100 r_g. The 2D plane created by the BH spin vector and the large-scale jet angular momentum vector is displayed, rotating the x–z plane by the corresponding jet precession angle $\varphi_0 = [0°, 28.4°, 42.2°]$ for `T0`, `T30`, and `T60`, respectively (given in Table 1). The red and black lines in all plots denote the magnetization, $b^2/\rho c^2 = 1$, and the Bernoulli parameter, $Be = 1.02$, contours, respectively.

Fig. 3 shows the radial profiles of the tilt $\mathcal{T}$ (top row) and precession $\mathcal{P}$ (bottom row) for the models `T30` (left column) and `T60` (right column), time-averaged over [99 960, 100 960] t_g, along with their 1σ standard deviation. This interval at such late times is chosen to allow the simulations to reach a quasi-steady state at least within the inner 100 r_g. We average the radial profiles over 1000 t_g in order to average over the short time-scale variations in the flow that otherwise cause the angles to fluctuate at small radii. LT torques affect the near-BH region, with radial tilt oscillations in both the disc and the jet peaking at $r \sim$ 10–20 r_g (Figs 3a and c). This behaviour was shown previously for model `T30` by Liska et al. (2018) and is consistent with simulations of small misalignment (Fragile et al. 2007; White et al. 2019). The peak $\mathcal{T}$ values are close to 30°, instead of ∼40° at earlier times (5 × 10^4 t_g; Liska et al. 2018), suggesting gradual alignment of the disc over time, until the viscous spreading of the disc saturates. Figs 3(a) and (c) clearly show that the jet follows

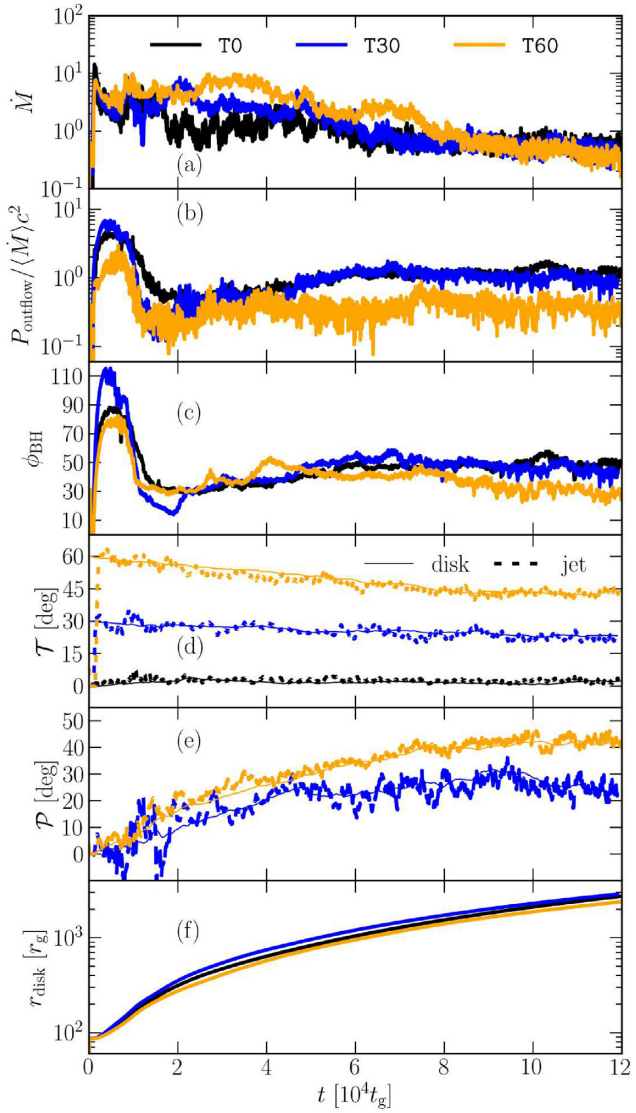

Figure 2. Time dependence of simulation quantities reveal how BH–disc systems evolve with varying initial misalignment angles, namely $\mathcal{T}_{\rm init} = 0°$ (T0), 30° (T30), and 60° (T60). The accretion rate, $\dot{M}$, is presented in normalized units (a), total outflow power $P_{\rm outflow}$ normalized by accretion rate (time-averaged over [99 960, 100 960] $t_{\rm g}$) (b), dimensionless magnetic flux $\phi_{\rm BH}$ in Gaussian units (c), with all quantities calculated at the event horizon. We also show the tilt angle $\mathcal{T}(t)$ and precession angle $\mathcal{P}(t)$ (d and e) of the disc, along with the jet for models T30 and T60, as $\mathcal{P}$ for $\mathcal{T}_{\rm init} = 0°$ is not well-defined. Both the angles are radially averaged over [50, 150] $r_{\rm g}$. It is noteworthy that the jet orientation is more variable than that of the disc. The barycentric radius of the disc $r_{\rm disc}$ (equation 6) (f) shows that all three models display similar viscous spreading, and therefore indicate similar rates of outward angular momentum transfer.

the disc orientation at larger radii, and therefore the large-scale jet is always misaligned with respect to the BH spin direction, while the inner jet undergoes a small degree of alignment. This result is similar to the conclusions of McKinney et al. (2013), who considered misalignment under MAD conditions. However, this contradicts the assumption by White et al. (2020) that the jets follow the BH spin direction at large radii. This assumption can significantly affect the orientation of the BH images as the inferred observer inclination depends on the jet orientation in the sky (see Section 4.2). In this

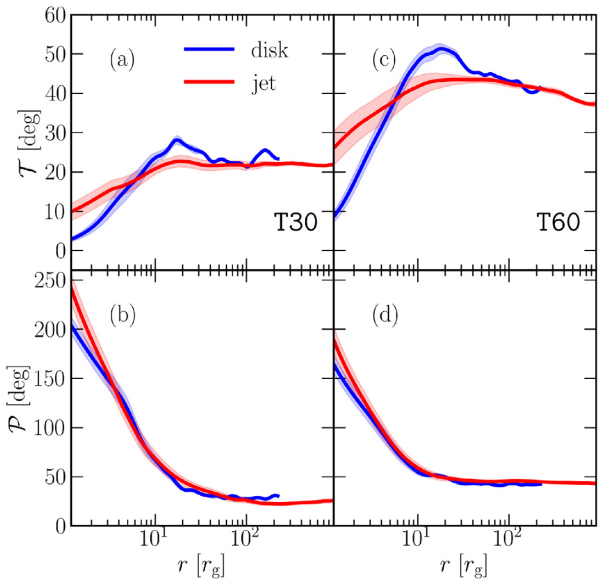

Figure 3. Misaligned discs show disc warping and jet bending. We show, for models T30 (a and b) and T60 (c and d), the tilt angle $\mathcal{T}$, time-averaged over [99 960, 100 960] $t_{\rm g}$, plotted with 1σ deviation (a,c). The precession angle $\mathcal{P}$, with the 1σ deviation (b,d) illustrates that the inner disc precesses much more than the outer disc and hence displays a twist in the disc. The inner parts of both the disc and the jet are quite variable as indicated by the extended shaded regions. We hereafter redefine the $\varphi = 0°$ plane as the plane in which the BH spin vector and the large-scale jet angular momentum vector resides for each individual simulation.

work, we have considered relatively powerful jets with $\phi_{\rm BH} \gtrsim 30$ (Table 1) as compared to White et al. (2019), where $\phi_{\rm BH} \lesssim 8$, assuming that all the magnetic flux goes into powering the jets ($P_{\rm outflow} \propto \phi_{\rm BH}^2$; Blandford & Znajek 1977; Tchekhovskoy, Narayan & McKinney 2010).

Henceforth, we will refer to the plane of the BH spin and the jet angular momentum vector, i.e. the 2D cross-section shown in Fig. 1, as the reference $\varphi = 0°$ plane, which would be useful as a notation for the BH images in the next section.

3.1 GRRT imaging: synchrotron maps and SEDs

In jet observations, the inclination (θ_0) is usually defined as the angle between the observer's line of sight and the large-scale jet. We therefore align our camera position according to the jet tilt $\mathcal{T}$ and precession $\mathcal{P}$ angles, spatially and temporally averaged between [50, 150] $r_{\rm g}$ and [99 960, 100 960] $t_{\rm g}$. For our observer camera, we redefine the spherical grid: the $\varphi_0 = 0°$ plane is equivalent to the GRMHD $y = 0$ plane rotated by the corresponding precession $\mathcal{P}_{\rm j}$ angle (Table 1), and the polar axis, i.e. the $x = y = 0$ line, is rotated by the corresponding tilt angle $\mathcal{T}_{\rm j}$. Therefore, we now have a camera grid which is aligned with the large-scale jet. Note that the precession angle is undefined for non-tilted jets (e.g. White et al. 2019), hence we took $\mathcal{P}_{\rm j} = 0°$ for T0. The camera field of view (FOV) is set to be $75\,r_{\rm g} \times 75\,r_{\rm g}$, which is sufficient since warping occurs within $r \lesssim 20\ r_{\rm g}$, while the image resolution is 1024 × 1024 pixels. For a BH with the same mass and at the same distance as M87, 100 $r_{\rm g}$ corresponds to 382 micro-arcseconds (μas), which corresponds to an FOV of 286.5 μas. The simplest example to showcase the alignment of the camera grid with the large-scale jet is when we observe our

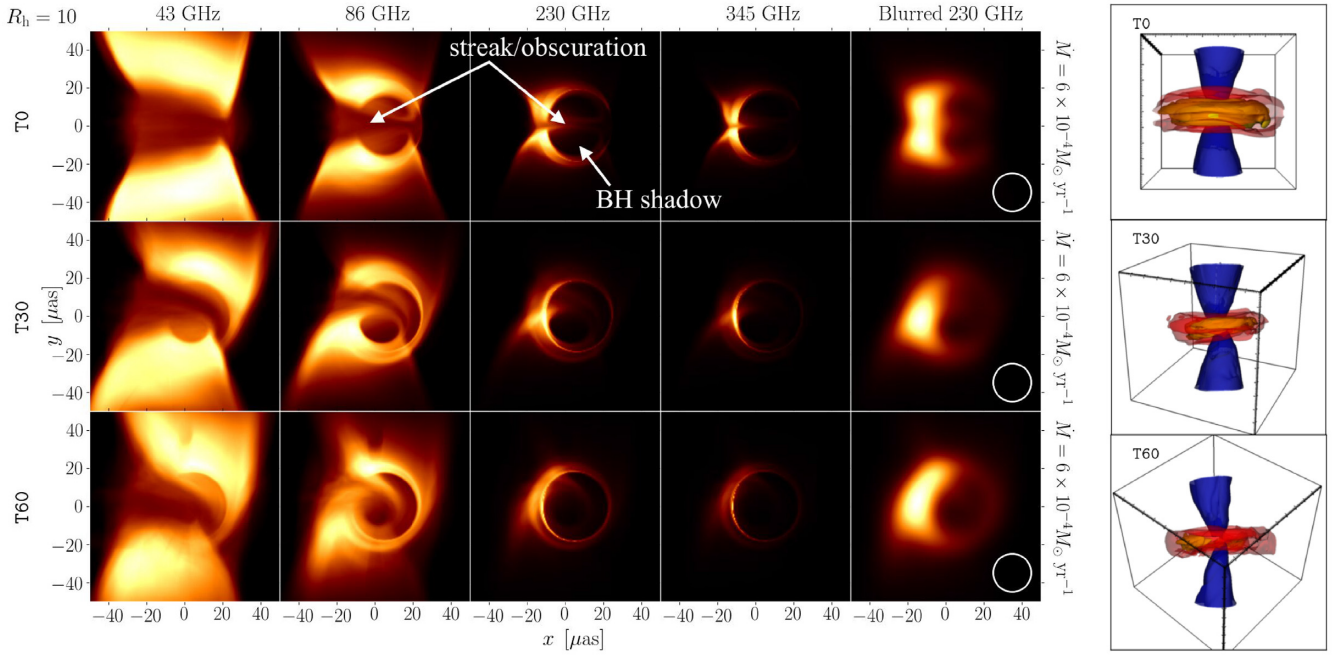

Figure 4. Left figure: Time-averaged, edge-on synthetic GRRT images of misaligned BH disc/jet systems using $R_h = 10$ for the electron temperature prescription (see equation 1), scaled to M87 at a constant accretion rate $\dot{M} = 6 \times 10^{-4}$ $M_\odot$ yr^{-1}, calculated over [99 960, 100 960] t_g and zoomed-in to the inner 100×100 μas^2 region. The observer is positioned edge-on relative to the large-scale disc using the disc tilt and precession angle values from Fig. 3, i.e. (θ_0, φ_0)=(90°, 0°). The colour scale is linear and normalized to unity for each image. From left to right: images at frequencies of 43, 86, 230, and 345 GHz, along with the 230 GHz image convolved with a Gaussian beam (full width at half-maximum of 20 μas). From top to bottom: synthetic observable GRRT images with initial tilt angles of 0° (`T0`), 30° (`T30`), and 60° (`T60`). Rightmost figure: 3D density contour plot visualizations for (top to bottom): `T0`, `T30`, and `T60`, respectively, as viewed at the same observer position as for the GRRT images. Dimensions are indicated by a bounding cube of size 50 r_g. The corresponding cases for $R_h = (1, 100)$ are shown in Appendix A.

disc–jet system at an inclination of $\theta_0 = 90°$ (i.e. edge-on to the outer disc).

Fig. 4 shows synthetic mm-radio images for $R_h = 10$ applied to an M87-like disc/jet system at an accretion rate of 6×10^{-4} $M_\odot$ yr^{-1}, with the observer positioned perpendicular to the jet axis (or edge-on to the large-scale disc) at four frequencies: 43, 86, 230, and 345 GHz. We have chosen $R_h = 10$, which yields contributions from both the disc and the jet to the total emission. We also show the 3D visualizations of the disc/jet system in the rightmost column of Fig. 4, as observed from the same direction as the GRRT camera. The rotating accretion flow surrounding the BH is clearly visible in the 43 and 86 GHz images (Fig. 4, left: first and second columns). At higher tilts, the inner part of the bottom jet bends towards the observer and is Doppler-boosted. This bending is visible as observing frequency is increased to 230 and 345 GHz, where the inner regions of the accretion flow closest to the BH are probed (Fig. 4, third and fourth columns). The dark (or flux depressed) circular region in the image centre is due to gravitational lensing by the BH and is a characteristic of images of accreting BHs (Narayan, Johnson & Gammie 2019). Hereafter, we refer to this flux depressed region as the BH 'shadow' (see Fig. 4). If we focus at the centre of the `T0` 230 GHz image (third from left in the top row of Fig. 4), we see that the BH shadow is obscured by a thin 'streak'-like shaped feature. This feature, hereafter referred to as the 'streak', is the flux originating from the plunging streams, which begin at the innermost stable circular orbit (or ISCO) for an aligned disc (`T0`) and further out for the case of the tilted runs (Fragile et al. 2007). This streak shines more brightly for `T0` as the emission is boosted towards the observer, whereas in the case of `T30` and `T60`, the inner disc is bent with respect to the outer disc, with the flow no longer being directed towards the observer. Such a curved streak is therefore an indication of disc tilt, given that we know the jet direction, and could potentially be important for interpreting future EHT images of Sgr A*, for which the inclination is a matter of much debate, with semi-analytical modelling (assuming a jetted model) favouring higher inclinations (e.g. Markoff, Bower & Falcke 2007; Connors et al. 2017), GRMHD simulations opting for both high (e.g. Mościbrodzka et al. 2009; Shcherbakov, Penna & McKinney 2012; Drappeau et al. 2013) as well as intermediate (∼30°−60°) inclinations (e.g. Dexter et al. 2010; Mościbrodzka & Falcke 2013; Davelaar et al. 2018) and, more recently, Gravity Collaboration (2018) inferred low inclinations $\lesssim$30°.

We see that the streak becomes progressively more optically thick at lower frequencies. Imaging at 86 GHz, where this feature is most distinguishable among the selected frequencies, may be essential for capturing possible disc/jet warps due to misalignment. At 86 GHz, Issaoun et al. (2019) has shown that combining the imaging power of the Global Millimetre VLBI Array (GMVA) and the Atacama Large Millimetre/submillimetre Array (ALMA) results in constraining the size and structure of the central emitting region in Sgr A* to an impressive limit. Further constraints from the anticipated EHT Sgr A* 230 GHz images will be vital in capturing possible disc misalignment. We also show GRRT images of our models at different inclination angles later on in Section 4.3 and Appendix C. In Appendix A1, we show sets of images for disc-dominated emission ($R_h = 1$; Fig. A1) and jet-dominated emission ($R_h = 100$; Fig. A2). With higher R_h values, the disc electron temperature drops and the jet becomes more visible with respect to the disc. Due to the decrease

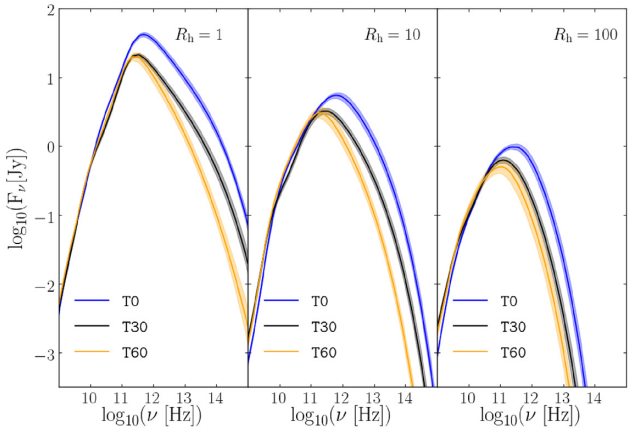

Figure 5. The resultant SEDs for misaligned BH disc/jet systems viewed edge-on to the outer disc (Fig. 4) show that with increasing R_h, the peak flux decreases, but the low-frequency emission does not vary with increasing misalignment even though misalignment introduces a Doppler-boosted inner jet (Fig. 4). The GRRT images are scaled to M87 at an accretion rate of $6 \times 10^{-4}\,M_\odot\,yr^{-1}$. From left to right: SEDs for increasing R_h values for each of models `T0`, `T30`, and `T60`.

in disc electron temperature, the streak feature also diminishes in brightness at 230 and 345 GHz.

Fig. 5 shows the corresponding spectral energy distribution (SED) generated for each model for the three different values of R_h. Since the mass and distance scales, as well as the accretion rate, are fixed for this set of GRRT images, higher R_h values result in lower peak synchrotron fluxes. Viewing from edge-on with respect to the disc, for higher tilts the aforementioned warping causes one of the inner jets ($r \lesssim 20\ r_g$) to point towards the observer and the other jet to point away, as seen from Figs 4 and A2. Hence, the net radio emission remains roughly similar for the three tilted models at the same R_h. For larger misalignment angles, the models have lower synchrotron peaks with a shift of the peak towards the radio as well as lower near-infrared (NIR) and optical emission. Hence for an edge-on BH disc/jet system, the disc/jet warp creates a substantial change in the image as well as the SED. Note that, instead of using a constant accretion rate, if we were to fit to the same flux at the EHT frequency (i.e. 230 GHz), the accretion rate would have to be higher for the tilted models and hence the radio flux would also be higher, while the NIR/optical emission will be quite similar between the three models. Additionally, for the case of Sgr A*, a higher accretion rate would change the predicted X-ray emission due to synchrotron self-Compton (SSC) emission. Consequently, such tilted models may be ruled out by comparing to quiescent Sgr A* X-ray spectra.

3.2 The case of M87

In this section, we apply our tilted models to M87 (EHTC 2019a). To match the crescent position in the M87 image as well as the direction of the jet, EHTC (2019b) found that for a positive BH spin ($a > 0$), the observer inclination angle $\theta_0 > 90°$. From the jet/counter-jet flux intensity ratio at 43 GHz, Mertens et al. (2016) estimated that the jet is $\sim$17° offset to our line of sight (i.e. the viewing angle). Using these two results, we chose an inclination angle of $\theta_0 = 163°$, i.e. 17° offset from the jet moving in the opposite direction to the BH spin vector, such that we view the disc material to rotate clockwise. Hence, for M87, we shift our camera position to $\theta_0 = 163°$ for each of the different tilt cases, with the jet direction given by the time-averaged tilt $\mathcal{T}_j$ and precession $\mathcal{P}_j$ angles from Table 1. As a first exploration of the simulations, in this section we restrict ourselves to the observer's line of sight being in the plane shared by the large-scale jets and BH spin axes (later we will relax this condition). This still leaves two possible configurations: one where the BH spin vector and the bottom jet reside in the same half of the image plane ($\varphi_0 = 0°$) and the other where the BH spin vector and the bottom jet are in opposite halves ($\varphi_0 = 180°$). We find that $\varphi_0 = 180°$ is more favourable since the forward jet must appear on the right-hand side of the synthetic image plane while keeping the crescent shape in the bottom half of the image. This choice does not make a difference for the `T0` case, since the jet is roughly axisymmetric. Furthermore, we rotate the image to match the M87 outer-jet position angle of PA = 288° (Walker et al. 2018).

Fig. 6 shows the GRRT M87 images for $R_h = 10$, time-averaged over [99 960, 100 960] t_g, with the accretion rate for each model set to match the 221 GHz flux shown in the M87 SED (Fig. 7). The synchrotron maps and SEDs have the same FOV and resolution as quoted in the previous section. The shadow size is about 40 μas as expected. However, due to the disc warp, some flux is present in front of the shadow for both misaligned models, which may itself be a crucial diagnostic since the brightness ratio from the ring to the depression (i.e. the shadow region) is expected to be increasingly better measured with future EHT observations. The extent of the southern bright crescent in the blurred 230 GHz image becomes smaller with increasing tilt angle. It is particularly noteworthy that the asymmetry in the upper and lower halves of the photon ring increases with increase in tilt. However, both of these features depend on the underlying electron temperature distribution, and therefore investigation of more sophisticated treatments, e.g. two-temperature plasma physics (e.g. Chael et al. 2018), is required.

The $R_h = 1$ and $R_h = 100$ cases are shown in Appendix A2, namely, Figs A3 and A4. The plunging region becomes more visible with increasing tilt angle as the streak in front of the shadow grows more distinct, similar to tilted models seen in Section 3.1 with larger value of R_h. Since the disc and jet at low radii display a smaller tilt and larger precession angle as compared to the large-scale jet (see Fig. 3), a part of the disc/jet is slightly warped towards the observer and lensing effects no longer completely dominate the 230 GHz synthetic image. A notable difference from previous work is the absence of the bright 'double' crescent feature, one on each side of the shadow, seen in face-on images of tilted discs (Dexter & Fragile 2013, Fig. 5). This double crescent structure was attributed to standing shocks in the plunging region for tilted disc models in Fragile et al. (2007). Considering that White et al. (2020), who used similar parameters to Fragile et al. (2007), also found the double crescent feature to be absent, this leads us to speculate that such strong standing shock features as seen by Dexter & Fragile (2013) might stem from a difference in grid resolution and/or the numerical methods, e.g. the shock-capturing scheme, employed in the different GRMHD codes, or could be a result of our assumed electron temperature model (used in the EHT M87 papers; EHTC 2019b), as suggested by White et al. (2020). In our models, the flow in the plunging streams is not subject to strong shock-heating, and therefore the ion temperature does not steeply rise in this region and there is no enhanced synchrotron emission. Hence, the plunging streams do not form the double crescent feature, but instead we see a single crescent feature consistent with Doppler boosting, without significant additional heating. Similar to the results of White et al. (2020), the change in the shape of the crescent feature with tilt translates to a change in the BH shadow shape as is evident from the blurred 230 GHz images in Fig. 6. Further, we note that the key

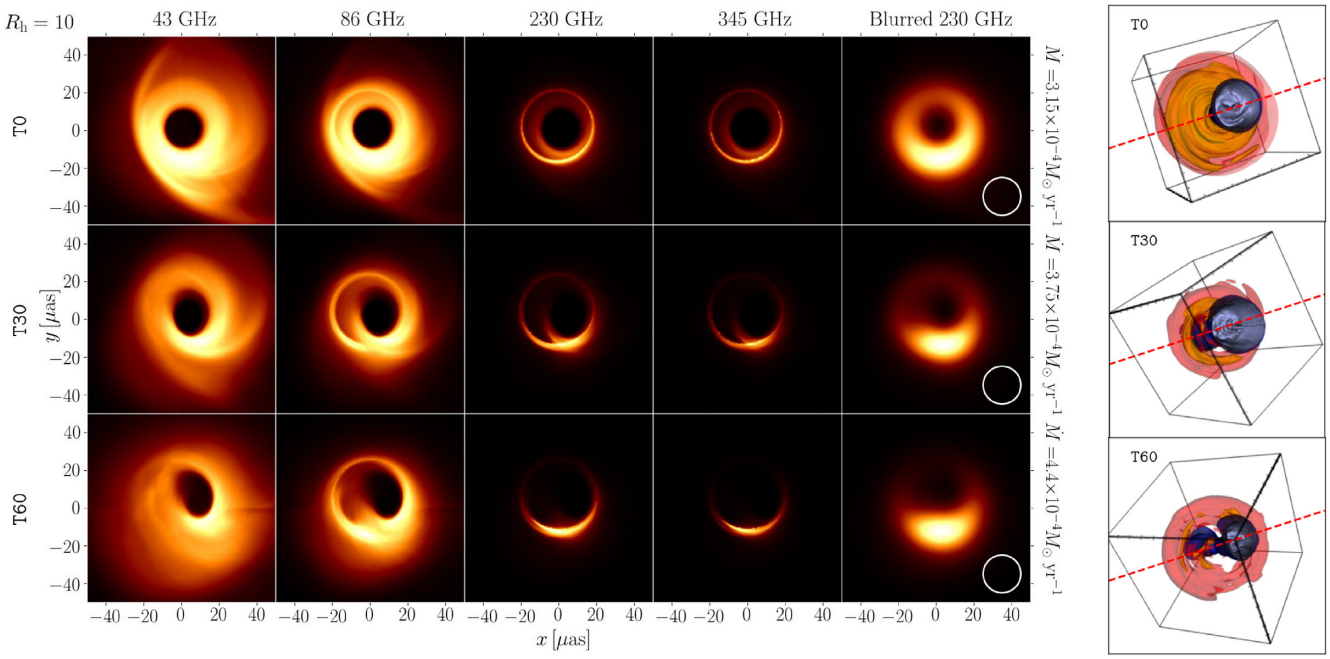

Figure 6. Left figure: Time-averaged, synthetic radio images of misaligned BH disc/jet systems using $R_h = 10$. The observer position is chosen such that the viewing angle is 17° offset from the direction of the large-scale bottom jet ($r \gtrsim 50\, r_g$), i.e. $(\theta_0, \varphi_0) = (163°, 180°)$, calculated over [99 960, 100 960] t_g. Images are rotated to fit the position angle PA = 288° of the large-scale jet in M87. From left to right: images at frequencies of 43, 86, 230, and 345 GHz, along with the blurred 230 GHz image (see Fig. 4). From top to bottom: underlying GRMHD simulations with initial tilt angles of 0°, 30°, and 60°. Rightmost figure: density contour plot visualizations for (top to bottom) `T0`, `T30`, and `T60` viewed at the same observer position as for the synthetic GRRT images and rotated to fit the large-scale jet position angle PA = 288° (red dashed line).

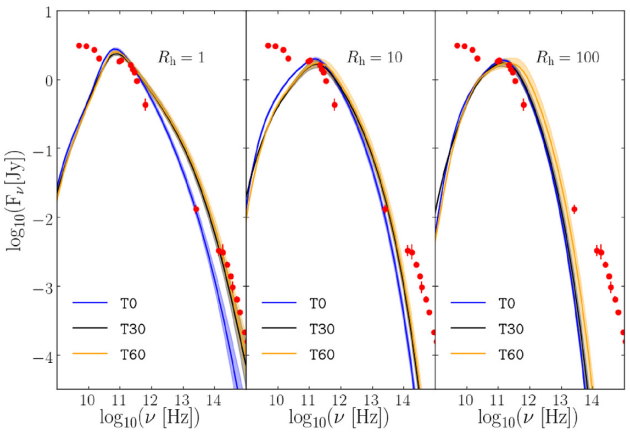

Figure 7. SEDs for misaligned BH disc/jet systems applied to M87 (Fig. 4) show little change with increasing R_h. The GRRT images are scaled to M87 with an accretion rate chosen to fit for the 221 GHz data point in the SED. From left to right: SEDs for increasing R_h values for each of models `T0`, `T30`, and `T60`. The radio, sub-mm, infrared, and optical data points are taken from Prieto et al. (2016).

element in calculating the above M87 images is the orientation of the jet, which undergoes some alignment towards the BH spin direction, but at larger scales ($r \gtrsim 50\, r_g$), clearly follows the disc orientation (see Fig. 3). Not accounting for the misalignment of the jet can have definite consequences for the 43 GHz jet position angle PA, which Walker et al. (2018) determined to be PA = 288°. As will be seen in Section 4.3, one can obtain excellent matches to the EHT M87 image for a variety of camera positions if the 43 GHz image is not used as a constraint.

The accretion rate used for each R_h tilt model is set by fitting the corresponding time-averaged SED to the 221 GHz data point (Fig. 7). The SED shows that the `T0` case displays higher emission at low frequencies as the jet at low radii is pointing towards the observer, whereas for the tilted models, the jet undergoes bending towards the observer over $r \lesssim 20\, r_g$.

4 DISCUSSION

4.1 Time series analysis of the M87 GRRT images

Fig. 8 shows the 230 GHz light curve derived from the core-unresolved spectrum (Fig. 7) for each tilt model at $R_h = 1$, 10, and 100, applied to the case of M87. The `T0` model shows the least amount of variation at 230 GHz due to strong gravitational lensing effects, irrespective of the temperature prescription, and is consistent with the results of EHTC (2019b). For the `T30` case, the variability is also small, except for a roughly monotonic flux increment for $t > 245$ d due to a flaring event. It is interesting to see that this flux increase in `T30` is more prominent for $R_h = 10$ and 100, since the jet plays a greater role in the net flux at higher R_h values. Overall, `T60` consistently displays the largest 1σ deviation (>10 per cent) over the chosen time period for a given R_h model, with a maximum factor of two change in the 230 GHz flux (see Table 2). This is a result of the turbulent inflow (outflow) in the disc (jet) being partially directed towards the observer. Hence the variability amplitude of the 230 GHz light curve may provide a diagnostic of disc misalignment in M87 and, perhaps, other AGNs. Future timing analysis of M87 EHT data may shed further light on whether there is indeed a tilted disc present.

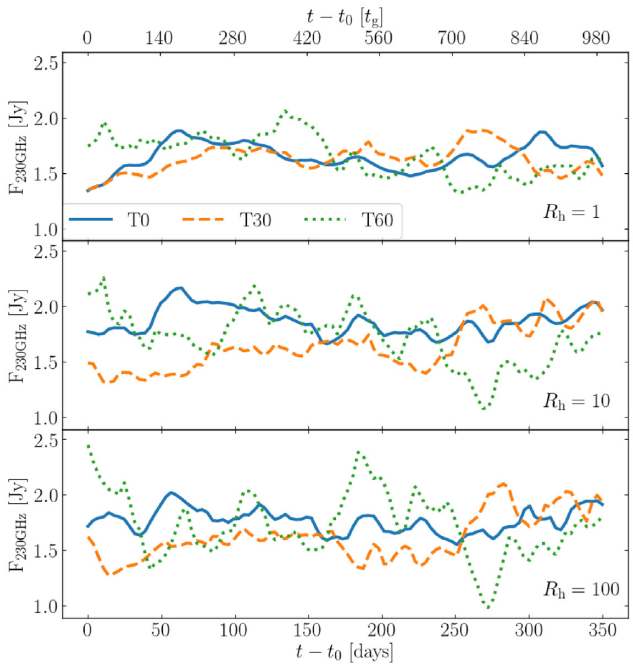

Figure 8. Higher tilts show more variability in the near-horizon flux when applied to the M87 BH. The 230 GHz light curve is shown over 1000 t_g, equivalent to 353.55 d when scaled to M87, or roughly one year, for models: `T0`, `T30`, and `T60` using (from top to bottom) R_h values of 1, 10, and 100, respectively. The start time $t_0 = 99970.58\, t_g \equiv 35354.92$ d. `T0` shows the least amount of variation as most of the 230 GHz flux is dominated by gravitational lensing effects rather than disc turbulence, while `T60` shows a flux change by a factor of more than 2 over the entire time period.

Table 2. Higher disc–BH misalignment results in a more variable 230 GHz light curve. We show the time-averaged fluxes from the 230 GHz light curve for each tilt and R_h model (see Fig. 8) as well as the 1σ standard deviation normalized by the averaged flux. `T0` shows the lowest deviation, while `T60`, the highest, indicating that deviations $\gtrsim$10 per cent might be a hint of possible misalignment.

	$\langle F_{230GHz}\rangle^{\max[F_{230GHz}]-\langle F_{230GHz}\rangle}_{\min[F_{230GHz}]-\langle F_{230GHz}\rangle}$		
Model	$R_h = 1$	$R_h = 10$	$R_h = 100$
`T0`	$1.649^{+0.232}_{-0.307}$	$1.864^{+0.302}_{-0.203}$	$1.765^{+0.257}_{-0.214}$
`T30`	$1.624^{+0.26}_{-0.274}$	$1.633^{+0.443}_{-0.32}$	$1.622^{+0.477}_{-0.349}$
`T60`	$1.656^{+0.402}_{-0.329}$	$1.723^{+0.532}_{-0.644}$	$1.727^{+0.721}_{-0.744}$

In Appendix B, we perform further analysis on the flux variability time-scales for each light curve and construct the power spectrum as well as the structure function. All of the models show substantial variability over time-scales ranging from days to months, with the fractional root mean square (rms) amplitude $\approx$7−16 per cent. We then model the power spectra and the structure function to find that the characteristic time-scale, i.e. the time-scale at which the variability transitions from red noise on short time-scales to white noise on long time-scales. The best-fitting characteristic time-scales from the power spectra and the structure functions are roughly of the order of a hundred days and a few tens of days respectively, as compared to the time-scale of ∼45 d obtained by Bower et al. (2015) where the 230 GHz light curve of M87 spanned over 10 yr. Due to the short duration of our light curves, we only capture the short time-scale

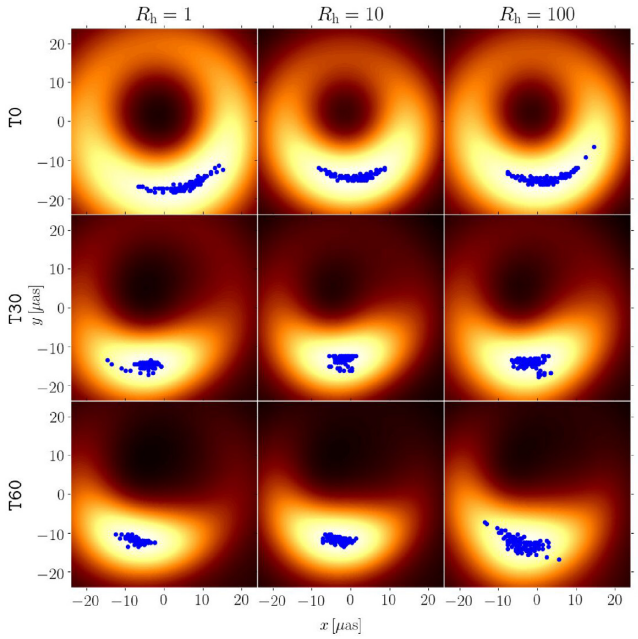

Figure 9. The location of the brightest pixel in the synthetic 230 GHz M87 images varies the most for `T0`. We show the brightest pixel locations (blue circles) over time against a background of the average blurred 230 GHz image for each of the nine models considered in this work. Note that each blue dot represents a different time snapshot. Top to bottom: tilt models `T0`, `T30`, and `T60`. Left to right: R_h =1, 10, and 100 models for the electron temperature prescription. For the `T0` case, gravitational lensing dominates the emission and hence turbulence in the flow changes the brightest spot location considerably. Doppler boosting of the plunging stream dominates the tilted images, which creates a preferential zone that points towards the observer where the boost is the maximum, and hence restricts the brightest spot location.

variability, with the power spectra well modelled by the characteristic slope =−2 of red noise (see Appendix B for more details).

Fig. 9 shows the spread of the brightest pixel of the blurred 230 GHz image for each combination of initial tilt and the R_h parameter. For this figure, each time snapshot is convolved with a Gaussian filter of FWHM = 20 μas and the position of the brightest pixel in each resulting image is calculated. From this figure, `T0` displays the maximum positional variability, spread across the time-averaged southern crescent, which is a result of the rotation of the disc as well as the gravitationally lensed emission from the counter-jet. Misalignment introduces some constraint on the positional spread as seen in the second and third rows in Fig. 9, displaying models `T30` and `T60`. $R_h = 10$ results in the smallest spread in both radial and azimuthal directions on the image plane, since the inner regions of both the disc and jet dominates the emission at 230 GHz and hence the location of the jet–disc boundary along the plunging streams dictates the position of the brightest spot.

4.2 Best-fitting images for M87

In Section 3.2, we considered GRRT maps of misaligned jets observed at an inclination of 163° offset from the large-scale jet direction, fixing the observer position with respect to the BH spin and the jet. In this subsection, we relax this assumption and move the observer's position azimuthally around the bottom jet at an inclination of 163°, looking for the best fit-by-eye convolved images for each model relative to the 230 GHz M87 observations (EHTC

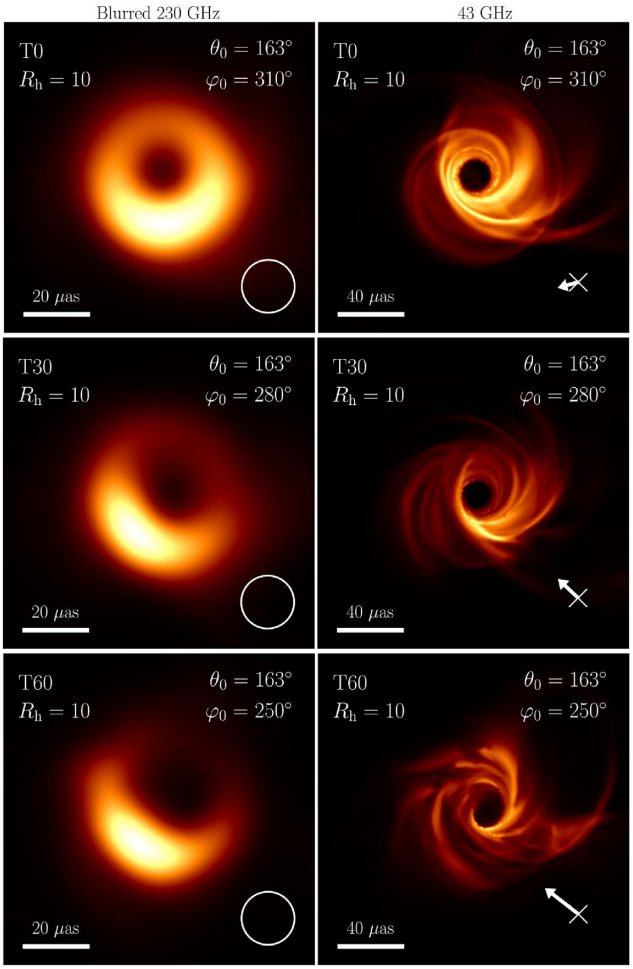

Figure 10. Comparing our models with the EHT M87 images indicates that M87 favourably hosts a misaligned disc and jet. We show the best fit-by-eye GRRT snapshot images from all three models when compared to the 230 GHz M87 BH image, with the 43 GHz jet pointed at PA ∼288° with $R_h = 10$. The BH spin direction and projection on to the image plane is also shown, with X meaning the BH spin is pointing into the plane. Best-fitting 230 GHz GRRT images of aligned BH models are consistent with the EHT M87 image to within 1.5σ. If this deviation persists with future EHT observations of M87, a misaligned disc/jet could become a more viable model for M87.

2019a), while ensuring that the 43 GHz jet image has a PA $\sim 288°$ (Walker et al. 2018). The accretion rate is taken to be the same as in Fig. 6. Fig. 10 shows the best fits for a single representative time snapshot (at $t = 100\,460\ t_g$) in the case of each tilt model. First, the tilted model images show significant dependence on the camera longitude φ_0 (see Section 4.3), since the underlying warped disc/jet is not axisymmetric. On the other hand, the aligned disc/jet model is roughly axisymmetric and so, the images are independent of the camera-φ_0, as expected.

Secondly, the best-fitting T0 230 GHz image (Fig. 10, first row, left column) has a PA offset with respect to the best-fitting EHT GRRT image (EHTC 2019b, Fig. 1, right-hand panel. EHTC (2019b) found that models with the spin vector of the BH oriented away from the observer ($\theta_0 \gtrsim 90°$) are favoured by comparing to both 230 and 43 GHz images of M87, which we also find. The statistically best-fitting 230 GHz images were found to have a mean PA in the range of $203°-209°$ (see Fig. 9 in EHTC 2019b) with a standard deviation of 54°, which means that aligned GRMHD simulations are consistent with the PA $\sim 288°$ found for the M87 jet at 43 GHz (Walker et al. 2018) within $\sim 1.5\sigma$. If we rotate our T0 230 GHz image so that we match the orientation of the 43 GHz M87 jet to the 43 GHz GRRT image, we find that the southern crescent is shifted to the bottom right quarter of the image, and hence does not match well with the EHT observed M87 image. Interestingly, disc misalignment provides more flexibility to fit the jet PA better as the crescent position is dependent on the choice of the camera longitude φ_0, as we mentioned above. Fig. 10 (second row) shows that for the T30 model, which possesses an average tilt angle of 22.7°, the image has a bright crescent shape located in the bottom left of the image at $\varphi_0 = 280°$ and fits remarkably well with the M87 jet PA, possibly hinting at the presence of a tilted disc in M87. Indeed, if the 230 GHz best-fitting aligned disc/jet model always resides at a 1.5σ deviation in PA away from the 43 GHz M87 jet PA over future EHT M87 observations, disc/jet misalignment in M87 could become a significant possibility.

Thirdly, the brightness asymmetry in the upper and lower halves of the photon ring increases with increasing misalignment (as mentioned above in Section 3.2). Using the crescent position and the ring brightness asymmetry in the 230 GHz image along with the jet PA orientation might help us to pinpoint the tilt angle of the jet, which can lead to better BH spin estimates. As an example, the T60 case appears more asymmetric by eye than the reconstructed images of M87, which leads us to favour smaller tilts. In this work, we propose that M87 possesses a disc with a misalignment $\lesssim 60°$, given the assumption that the BH spin is $a = 0.9375$ and the inclination angle is 17° offset to the large-scale bottom jet (i.e. the viewing angle). Images at frequencies lower than 230 GHz might provide more definitive proof of misalignment by directly capturing the disc warping region, located within roughly 20 r_g of the BH (see Fig. 3). However, the typical beam sizes for radio interferometric images at 43 and 86 GHz are presently too large to adequately resolve the inner 20 r_g. Imaging the jet base region with sufficient resolution to capture the warping of the disc and the jet as well as checking for time variability in the EHT observations (see Section 4.1) will go a long way towards testing our prediction of a tilted disc in M87.

4.3 Varying the observer inclination and longitude

Fig. 11 shows the blurred 230 and 43 GHz images for model T30 observed over a range of inclination angles, $\theta_0 = 180°-90°$, as well as also azimuthally rotating the observer around the large-scale bottom jet with $\varphi_0 = 0°-360°$, assuming $R_h = 10$ and scaled to M87 at an accretion rate of $3.75 \times 10^{-4}\ M_\odot\ yr^{-1}$ (see middle row of Fig. 6). Using this catalogue of images, we can pick out the best-fitting images as compared to the EHT M87 image. First, we see that ring brightness asymmetry constraint favours smaller inclinations, along with a few acceptable images at $\theta_0 \sim 45°$ and $\varphi_0 \lesssim 30°$ or $\gtrsim 330°$. If matching the jet PA to 288° and requiring the bright crescent to be in the bottom left of the image, higher φ_0 values are clearly favoured. This result shows that accounting for the large-scale jet orientation is crucial in constraining the acceptable values of θ_0 and φ_0. Secondly, at higher inclinations, the spectral shape for each tilt model is sufficiently distinguishable (see Fig. 5) and perhaps the M87 SED might be able to rule out some observer inclinations. Not only can we use these images to fit for M87, but given that Sgr A* extends over a similar angular size in the sky (due to comparatively close values for the ratio of the BH mass and the distance), we can also fit these images to upcoming EHT observations of Sgr A* in the same manner.

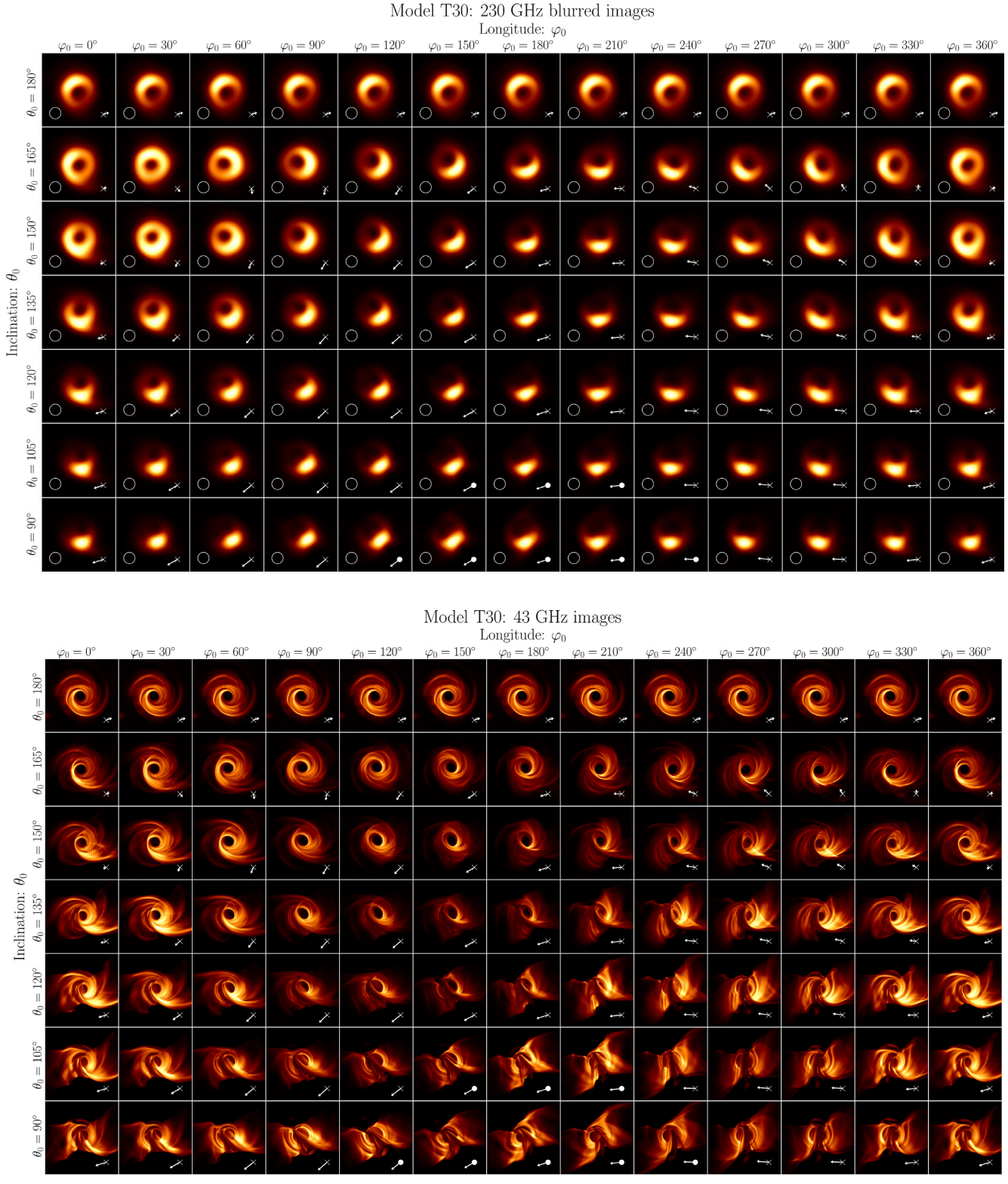

Figure 11. Images at 230 and 43 GHz for different values of the observer inclination θ_0 and longitude φ_0, for a single snapshot of model `T30` with $R_{\rm h} = 10$. The box sizes are 110×110 and 150×150 μas^2 for the 230 and the 43 GHz images, respectively. A strong dependence of the images on φ_0 due to the non-axisymmetric nature of the disc/jet warping is clearly seen. The BH spin vector direction is also shown with a white arrow and the X (O) indicating whether the BH spin vector is pointing into (out of) the image plane. The arrow length is indicative of the BH spin projection on to the image plane. The images have been rotated to fit the 43 GHz jet PA from Walker et al. (2018).

5 CONCLUSIONS

In this work, using our GPU-accelerated GRMHD code `h-amr`, we have simulated three BH accretion discs, with the disc mid-plane initially misaligned by 0°, 30°, and 60° with respect to the $z = 0$ plane. Using these three models, we calculated the first synthetic radio images of misaligned accretion disc/jet models scaled to the M87 BH mass, performing radiation transfer using the GRRT code BHOSS. Our analysis of the 230 GHz synthetic images suggests that M87* could host an accretion disc with a reasonably large misalignment angle ($\lesssim$60°). In light of these results, the misalignment angle, neglected in the current EHT theoretical models (EHTC 2019b), may therefore be an important additional parameter within the observational fitting procedure of GRMHD simulation models worthy of further exploration. Tilt brings about a change in the BH shadow appearance, which could be verified with future EHT observations of M87*. We note that, recently, White et al. (2020) considered the case of weakly magnetized misaligned discs and found similar results to our work.

Thisstudy has assumed that the emission originates solely from thermal synchrotron radiation, further assuming an electron temperature prescription which calculates the electron temperature from the GRMHD-based ion temperature. These assumptions play an important role in the appearance of the M87 230 GHz synthetic images and warrant further study in order to fully address the question of possible misalignment in M87. From semi-analytical modelling of the M87 spectra (e.g. Lucchini, Krauß & Markoff 2019), the 230 GHz emission is expected to have a significant non-thermal synchrotron contribution, describable by a hybrid thermal–non-thermal electron distribution function (e.g. Davelaar et al. 2019). As Lucchini et al. (2019) mention, the X-ray spectrum is more likely to be dominated by the non-thermal emission rather than by an SSC inner jet. Therefore, self-consistently accounting for both the EHT image characteristics and the X-ray spectra will be the most constraining avenue for modelling the mixed thermal/non-thermal synchrotron emission in M87. Our future work will include two-temperature physics, which would allow independent evolution of the electron and ion temperatures, and perhaps shall add an additional layer of complexity in the system (e.g. Ressler et al. 2015; Chael et al. 2018; Ryan et al. 2018). Finally, with promising new telescope additions to the EHT array in the near future and the possible advent of space-VLBI telescopes over the next few decades, resolving smaller scale structures close to the base of the jet will gradually become a reality, playing a key role in the search for a misaligned disc in M87 and other SMBH systems.

ACKNOWLEDGEMENTS

We thank Jason Dexter for interesting discussions and useful comments. We thank the anonymous referee for providing helpful suggestions on the text. This research was made possible by NSF PRAC awards no. 1615281 and OAC-1811605 at the Blue Waters sustained-petascale computing project and supported in part under grant no. NSF PHY-1125915. KC, SM, and DY are supported by the Netherlands Organization for Scientific Research (NWO) VICI grant (no. 639.043.513), ZY is supported by a Leverhulme Trust Early Career Research Fellowship, ML and MK were supported by the NWO Spinoza Prize, AT by Northwestern University and by National Science Foundation grants AST-1815304, AST-1911080, CH by the Amsterdam Science Talent Scholarship, and AI by a Royal Society University Research Fellowship. This research has made use of NASA's Astrophysics Data System.

DATA AVAILABILITY

Data used to plot the images in this work are available in Zenodo at http://doi.org/10.5281/zenodo.3757013.

REFERENCES

Balbus S. A., Hawley J. F., 1991, ApJ, 376, 214
Blandford R. D., Znajek R. L., 1977, MNRAS, 179, 433
Bower G. C., Dexter J., Markoff S., Gurwell M. A., Rao R., McHardy I., 2015, ApJ, 811, L6
Caproni A., Livio M., Abraham Z., Mosquera Cuesta H. J., 2006, ApJ, 653, 112
Chael A., Rowan M., Narayan R., Johnson M., Sironi L., 2018, MNRAS, 478, 5209
Chael A., Narayan R., Johnson M. D., 2019, MNRAS, 486, 2873
Chatterjee K., Liska M., Tchekhovskoy A., Markoff S. B., 2019, MNRAS, 490, 2200
Connors R. M. T. et al., 2017, MNRAS, 466, 4121
Davelaar J., Mościbrodzka M., Bronzwaer T., Falcke H., 2018, A&A, 612, A34
Davelaar J. et al., 2019, A&A, 632, A2
Dexter J., Fragile P. C., 2011, ApJ, 730, 36
Dexter J., Fragile P. C., 2013, MNRAS, 432, 2252
Dexter J., Agol E., Fragile P. C., McKinney J. C., 2010, ApJ, 717, 1092
Dexter J., Kelly B., Bower G. C., Marrone D. P., Stone J., Plambeck R., 2014, MNRAS, 442, 2797
Doeleman S. S. et al., 2008, Nature, 455, 78
Drappeau S., Dibi S., Dexter J., Markoff S., Fragile P. C., 2013, MNRAS, 431, 2872
EHTC, 2019a, ApJ, 875, L1
EHTC, 2019b, ApJ, 875, L5
EHTC, 2019c, ApJ, 875, L6
Emmanoulopoulos D., McHardy I. M., Uttley P., 2010, MNRAS, 404, 931
Fish V. L., Shea M., Akiyama K., 2020, Adv. Space Res., 65, 821
Fishbone L. G., Moncrief V., 1976, ApJ, 207, 962
Fragile P. C., Anninos P., 2005, ApJ, 623, 347
Fragile P. C., Blaes O. M., 2008, ApJ, 687, 757
Fragile P. C., Blaes O. M., Anninos P., Salmonson J. D., 2007, ApJ, 668, 417
Generozov A., Blaes O., Fragile P. C., Henisey K. B., 2013, ApJ, 780, 81
Gravity Collaboration, 2018, A&A, 618, L10
Greene J., Bailyn C. D., Orosz J. A., 2001, ApJ, 554, 1290
Hawley J. F., Guan X., Krolik J. H., 2011, ApJ, 738, 84
Hjellming R. M., Rupen M. P., 1995, Nature, 375, 464
Ingram A., Done C., Fragile P. C., 2009, MNRAS, 397, L101
Issaoun S. et al., 2019, ApJ, 871, 30
Ivanov P. B., Illarionov A. F., 1997, MNRAS, 285, 394
King A. R., Pringle J. E., 2006, MNRAS, 373, L90
Lense J., Thirring H., 1918, Phys. Z., 19, 156
Leung P. K., Gammie C. F., Noble S. C., 2011, ApJ, 737, 21
Liska M., Hesp C., Tchekhovskoy A., Ingram A., van der Klis M., Markoff S., 2018, MNRAS, 474, L81
Liska M., Chatterjee K., Tchekhovskoy A., Yoon D., van Eijnatten D., Hesp C., Markoff S., Ingram A., van der Klis M., 2019a, preprint (arXiv: 1912.10192)
Liska M., Tchekhovskoy A., Ingram A., van der Klis M., 2019b, MNRAS, 487, 550
Liska M., Hesp C., Tchekhovskoy A., Ingram A., van der Klis M., Markoff S. B., Van Moer M., 2020, MNRAS
Lubow S. H., Ogilvie G. I., 2000, ApJ, 538, 326
Lucchini M., Krauß F., Markoff S., 2019, MNRAS, 489, 1633
Maccarone T. J., 2002, MNRAS, 336, 1371
Markoff S., Bower G. C., Falcke H., 2007, MNRAS, 379, 1519
McKinney J. C., Tchekhovskoy A., Blandford R. D., 2013, Science, 339, 49
Mertens F., Lobanov A. P., Walker R. C., Hardee P. E., 2016, A&A, 595, A54
Mościbrodzka M., Falcke H., 2013, A&A, 559, L3

Mościbrodzka M., Gammie C. F., Dolence J. C., Shiokawa H., Leung P. K., 2009, ApJ, 706, 497
Mościbrodzka M., Falcke H., Shiokawa H., 2016, A&A, 586, A38
Narayan R., Igumenshchev I. V., Abramowicz M. A., 2003, PASJ, 55, L69
Narayan R., Johnson M. D., Gammie C. F., 2019, ApJ, 885, L33
Palumbo D. C. M., Doeleman S. S., Johnson M. D., Bouman K. L., Chael A. A., 2019, ApJ, 881, 62
Papaloizou J. C. B., Lin D. N. C., 1995, ARA&A, 33, 505
Park J., Hada K., Kino M., Nakamura M., Ro H., Trippe S., 2019, ApJ, 871, 257
Pasham D. R. et al., 2019, Science, 363, 531
Polko P., McKinney J. C., 2017, MNRAS, 464, 2660
Porth O. et al., 2019, ApJS, 243, 26
Prieto M. A., Fernández-Ontiveros J. A., Markoff S., Espada D., González-Martín O., 2016, MNRAS, 457, 3801
Ressler S. M., Tchekhovskoy A., Quataert E., Chandra M., Gammie C. F., 2015, MNRAS, 454, 1848
Ressler S. M., Tchekhovskoy A., Quataert E., Gammie C. F., 2017, MNRAS, 467, 3604
Roelofs F. et al., 2019, A&A, 625, A124
Russell T. D. et al., 2019, ApJ, 883, 198
Ryan B. R., Ressler S. M., Dolence J. C., Gammie C., Quataert E., 2018, ApJ, 864, 126
Shcherbakov R. V., Penna R. F., McKinney J. C., 2012, ApJ, 755, 133
Sorathia K. A., Krolik J. H., Hawley J. F., 2013, ApJ, 777, 21
Stella L., Vietri M., 1998, ApJ, 492, L59
Tchekhovskoy A., McKinney J. C., 2012, MNRAS, 423, L55
Tchekhovskoy A., Narayan R., McKinney J. C., 2010, ApJ, 711, 50
Tchekhovskoy A., Narayan R., McKinney J. C., 2011, MNRAS, 418, L79
van den Eijnden J., Ingram A., Uttley P., Motta S. E., Belloni T. M., Gardenier D. W., 2017, MNRAS, 464, 2643
Volonteri M., Madau P., Quataert E., Rees M. J., 2005, ApJ, 620, 69
Walker R. C., Hardee P. E., Davies F. B., Ly C., Junor W., 2018, ApJ, 855, 128
White C. J., Quataert E., Blaes O., 2019, ApJ, 878, 51
White C. J., Dexter J., Blaes O., Quataert E., 2020, ApJ, 894, 14
Younsi Z., Wu K., Fuerst S. V., 2012, A&A, 545, A13
Younsi Z., Zhidenko A., Rezzolla L., Konoplya R., Mizuno Y., 2016, Phys. Rev. D, 94, 084025
Younsi Z., Porth O., Mizuno Y., Fromm C., Olivares H. 2020, Proceedings of the International Astronomical Union, 342, 9–12

APPENDIX A: CONSIDERING DISC- AND JET-DOMINATED EMISSION

Here, we discuss the GRRT images for $R_{\rm h}$ values of 1 and 100, for the two observer positions mentioned in the text, namely, edge-on to the outer disc in Section 3.1 and 17° offset to the bottom large-scale jet in Section 3.2.

A1 Edge-on case

For $R_{\rm h} = 1$, we have disc-dominated emission as the electron temperature is set to be the same as the ion temperature (see equation 1), which is higher in the disc as compared to the jet. The disc warp is visible as the outer accretion disc becomes increasingly optically thin, with the jet-dominated emission for $R_{\rm h} = 100$. Higher $R_{\rm h}$ images exhibit a curved streak similar to the one discussed above for $R_{\rm h} = 1$, but now offset from the shadow as the feature originates in the plunging streams and the jet edge.

A2 M87 case

The most prominent difference between $R_{\rm h} = 1$ and $R_{\rm h} = 100$ images lies in their brightest features at 43 GHz: the photon ring in the case

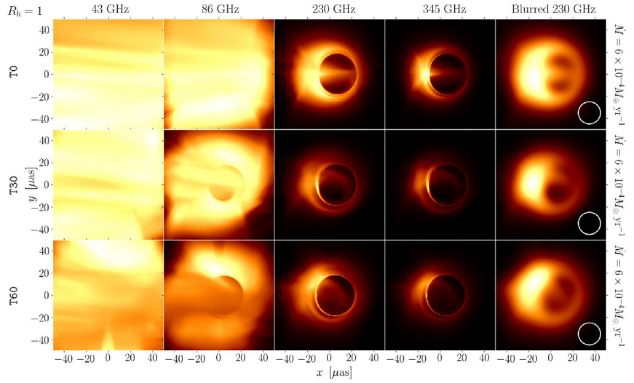

Figure A1. Time-averaged edge-on GRRT images of misaligned BH disc/jet systems using $R_{\rm h} = 1$ calculated over [99 960, 100 960] $t_{\rm g}$ and zoomed-in to the inner 100 × 100 μas^2 region. The camera is positioned at (θ_0, φ_0)=(90°, 0°). From left to right: images at frequencies of 43, 86, 230, and 345 GHz, along with the convolved 230 GHz image. From top to bottom: underlying models `T0`, `T30`, and `T60`. With $R_{\rm h} = 1$, the electron temperature is taken to be the same as that of the ion temperature everywhere, hence the disc shines brighter than the jet, which usually has a lower ion temperature.

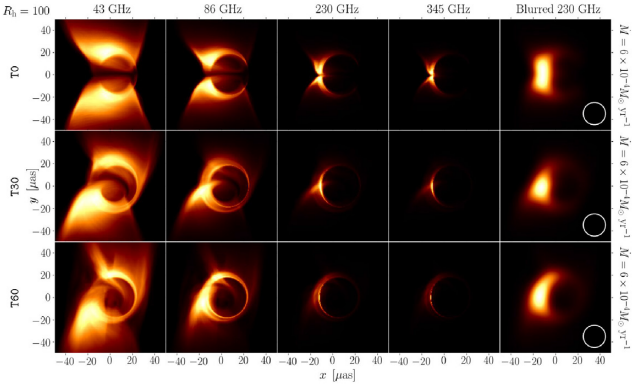

Figure A2. Same as Fig. A1 (edge-on case), but with $R_{\rm h} = 100$. Here, the jet contribution is more significant as the disc electron temperature is much smaller. The streak in front of the shadow is barely visible at 230 and 345 GHz, in contrast to Fig. A1.

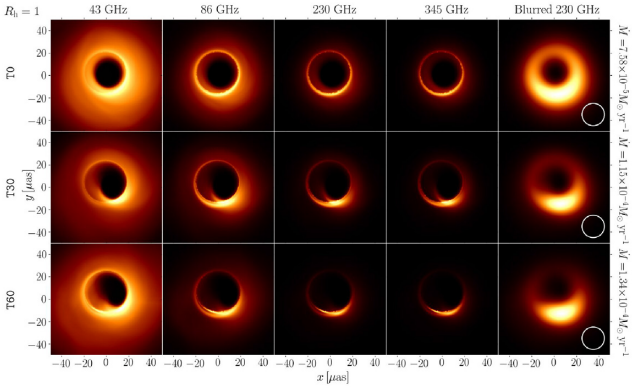

Figure A3. Time-averaged GRRT images of misaligned BH disc/jets targeted towards M87 (nearly face-on). Same as Fig. 6, but with $R_{\rm h} = 1$. For $R_{\rm h} = 1$, the disc emission dominates the image in the form of the photon ring, which is clearly distinguishable at all frequencies shown here. The blurred 230 GHz images look comparable to their $R_{\rm h} = 10$ versions, while at 43 GHz, there is almost no sign of the jet.

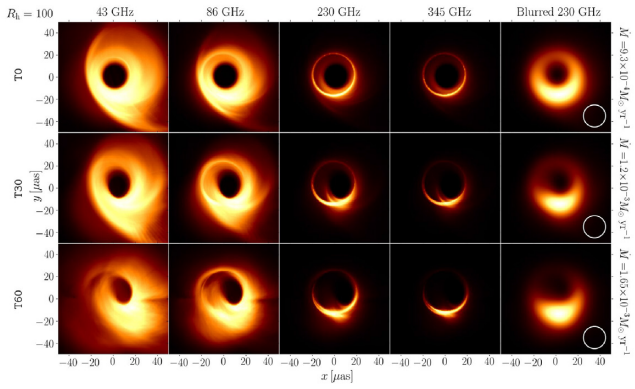

Figure A4. Same as Fig. A3 but with $R_h = 100$. The southern crescent is slightly extended for the tilted cases due to the boosted emission of the streak cutting across the face of the shadow. The dark feature seen in the righthand side of the 43 GHz image of `T60` is an artefact due to the jet sheath crossing the polar axis of the GRMHD grid.

of $R_h = 1$ and the extended streak in the case of $R_h = 100$. The 43 GHz image features an optically thick accretion flow in front of the shadow region, which is absent in the corresponding $R_h = 1$ image, indicating that the streak originates in the sheath region.

APPENDIX B: EXTENDED TIMING ANALYSIS: POWER SPECTRA AND STRUCTURE FUNCTIONS

In this section, we perform a Fourier transform of the 230 GHz light curves from Section 4.1 for our M87 models. Fig. B1 shows the fractional rms normalized power spectra for each of our models, using $R_h = 1$, 10, and 100. The cadence $(\Delta t)_{\rm min}$ of our images is $10\,t_g \equiv 3.54$ d, when scaled to M87, which enables us to capture the short time-scale variability in the emission. Each power spectrum can be well-fitted with a white noise component, where the power is independent of the variability frequency, and a red noise component, where the power scales as frequency^{-2}, smoothly joined together by a modified sigmoid function. The modified sigmoid function $S_{\rm var}$ is defined as a function of the variability frequency ($\nu_{\rm var} := 1/\Delta t$):

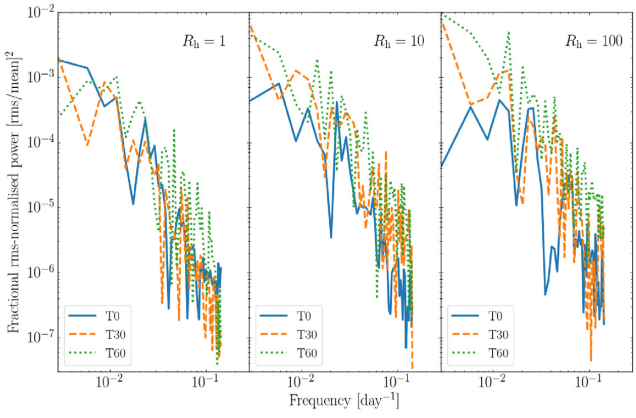

Figure B1. We show the fractional rms normalized power spectra for the 230 GHz M87 light curve for models `T0`, `T30`, and `T60` using $R_h = [1,\ 10,\ 100]$. We see that the short time-scale variability is described well by red noise (power $\propto$ frequency^{-2}). However, the long time-scale variability, characterized by white noise (power independent of frequency), is not captured due to the short time duration of our light curves.

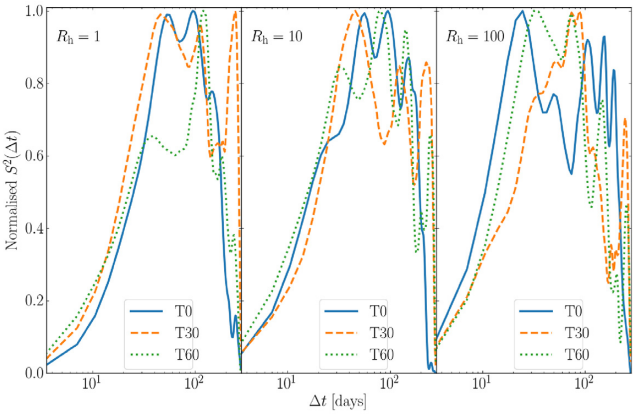

Figure B2. We show the structure function $S^2(\Delta t)$ (see equation B2) for each tilt and R_h model. The time-scale Δt spans from $10\,t_g \simeq 3.54$ to $1000\,t_g \simeq 354$ d. The structure functions look very similar except for model `T0` with $R_h = 100$, where the saturation to white noise seems to be achieved at shorter time-scales as compared to the other models. Additionally, structure functions suffer from a turnover at time-scales comparable to the time duration of the light curve, which is what we see for $\Delta t \gtrsim 150$ d.

Table B1. The fractional rms amplitude and best-fitting characteristic time-scale ($\tau_{\rm rms}$ in days) from the power spectra (Fig. B1) constructed from the 230 GHz M87 light curve for each disc/jet model and R_h model (Fig. 8). The rms (per cent) shows that higher tilt angles and more jet contribution in the emission result in larger variability, with the characteristic time-scale of a few 100 d. Each power spectrum is fitted with a white noise component and a red noise component, joined smoothly together by a modified sigmoid function (see equation B1). The best fit for $\tau_{\rm rms}$ is found using a least-squares method.

	rms (per cent), $\tau_{\rm rms}$ (d)		
Model	$R_h = 1$	$R_h = 10$	$R_h = 100$
`T0`	7.4, 202.6	6.5, 157.3	6.0, 43.6
`T30`	7.4, 130.7	12.4, 343.0	12.4, 343.0
`T60`	10.9, 86.0	14.2, 231.7	16.8, 228.1

$$S_{\rm var}(\nu_{\rm var}, n_{\rm var}) := \left\{1 + \exp\left[-(\tau_{\rm rms}\nu_{\rm var})^{n_{\rm var}}\right]\right\}^{-1}, \quad \text{(B1)}$$

where $\tau_{\rm rms}$ is defined as the characteristic time-scale where the variability transitions from red noise, which dominates at shorter time-scales, to white noise, which is more characteristic of long time-scales. We use $n_{\rm var} = 6$ to reduce the transition zone. Table B1 shows the fractional rms variability amplitude calculated from the power spectra and the corresponding characteristic transition time-scale $\tau_{\rm rms}$, determined using a least-squares fitting method. The overall trend is that with higher initial disc tilt, the rms-percentage (rms per cent) increases, while higher R_h values result in larger rms per cent as well (except for `T0`, where the rms per cent is relatively unchanged). This suggests that introducing disc misalignment and/or a higher jet contribution to the total emission results in more variability on longer time-scales. Of course, the caveat is that the slope of -2 for the power law is the steepest slope one can measure reliably with a boxcar window Fourier method (which is what we used), where steeper slopes (≤ -2) get converted to slope $=-2$ due to low-frequency leakage.

Bower et al. (2015) analysed the variability of M87's 1.3 mm ($\equiv$230 GHz) light curve over a period of 10 yr using the submillimetre array (SMA) and found the characteristic time-scale to be

Table B2. The best-fitting characteristic time-scale (τ_{sf} in days) from the structure functions (Fig. B2) constructed from the 230 GHz M87 light curve for each disc/jet model and R_h model (Fig. 8), fitted with equation (B3) using a least-squares method. The bounding box for the fitting is [3.54, 150] d, with the lower end indicating the cadence of the data sampling. The upper end is chosen such that we avoid the turnover of the structure function at time-scales comparable to the time duration of the light curve (∼1 yr).

Model	τ_{sf} (d) $R_h = 1$	$R_h = 10$	$R_h = 100$
T0	26.3	22.8	10.7
T30	14.0	33.1	34.9
T60	38.3	19.9	12.7

approximately 45^{+61}_{-24} d, modelling the light curve $s(t)$ as a damped random walk (DRW) process. They used a structure function $S^2(\Delta t)$ of the form

$$S^2(\Delta t) = \frac{1}{N}\sum[s(t) - s(t + \Delta t)^2], \tag{B2}$$

where N is the number of data points in the light curve and the summation is taken over all light-curve data points. Fig. 2 in Bower et al. (2015) showed that the structure function for M87 increases steadily on short time-scales due to red noise, saturating at long time-scales due to white noise. This structure function was modelled as

$$S^2_{DRW}(\Delta t) = S^2_\infty[1 - \exp(-\Delta t/\tau_{sf})], \tag{B3}$$

with S^2_∞ is the power in the light curve on long time-scales and τ_{sf} is the characteristic time-scale for the transition from red to white noise. Bower et al. (2015) used a Bayesian approach to model the light curve due to the noisy nature of observed data and irregular spacing of the data points in time (following Dexter et al. 2014).

Here, we choose to adopt the simpler approach of Chael, Narayan & Johnson (2019), since our sampling cadence is constant, and directly fit the structure functions (shown in Fig. B2) for each tilt and R_h model with equation (B3) using a least-squares method. Using this technique, we see that τ_{sf} is of the order of a few tens of days (Table B2), in stark contrast to the τ_{rms} values (Table B1). This result exposes the primary caveat of our modelling approach for both the power spectra and the structure functions: the short time duration of our analysed light curves. Fig. 9 of Chael et al. (2019) shows that white noise is achieved beyond time-scales of 300 d, while the light curves cover 4.8 yr, significantly longer than the duration of our light curves.

Emmanoulopoulos, McHardy & Uttley (2010) showed that one cannot reliably estimate time-scales with the structure function, which is illustrated by the incompatibility between τ_{sf} and τ_{rms}. Our power spectra from the year-long light curve cannot explain τ_{sf} values as we clearly have a sufficiently long-enough duration to see the noise transition from red to white on time-scales of 10–20 d, suggesting that the time-scales are longer than that given by the structure functions. However, we must note that we have very few power estimates at the lowest frequencies, and their statistical error (arising from the stochastic nature of the light curve) is equal to the powers themselves, which makes it difficult to find a good fit for the time-scale. Further, the use of least-squares minimization is unsuitable for finding the turnover frequency as the error distribution is exponential rather than Gaussian in behaviour. However, the least-squares technique is no doubt the most straightforward fitting method and provides good order-of-magnitude estimates.

APPENDIX C: A GLOSSARY OF IMAGES FROM OUR MODELS

Here, we provide a collection of images at 230 and 43 GHz for the aligned model T0 (Fig. C1) and misaligned model T60 (Fig. C2). Fig. C1 clearly shows that images for an aligned BH disc/jet system is independent of the camera longitude φ_0, while Fig. C2 further illustrates the powerful effect of misalignment of BH images, with more pronounced disc/jet warping as compared to Fig. 11.

We also note that the images for the camera inclination $\theta_0 = 0^\circ$ do not change with φ_0 due to the direction of the camera 'up' vector. In order to illustrate the orientation of the camera, we can consider an analogue of the situation: imagine a person walking on the surface of the Earth with their eyes always directed towards the North Pole. In this analogy, their feet are pointing downwards, towards the centre of the Earth: this vector can be thought of as the camera 'viewing' vector that is normal to the image plane, pointing into the plane. Their eyes are always looking straight ahead, towards North: this is the same as the camera 'up' vector which is the positive y-axis in each of our images. In each M87 image, the camera 'up' vector is rotated such that the large-scale GRMHD jet projected on to the image plane fits the M87 jet PA. At $\theta_0 = 0^\circ$ (i.e. at the North Pole), the definition of a longitude fails, and hence, changing φ_0 does not change the orientation of the image.

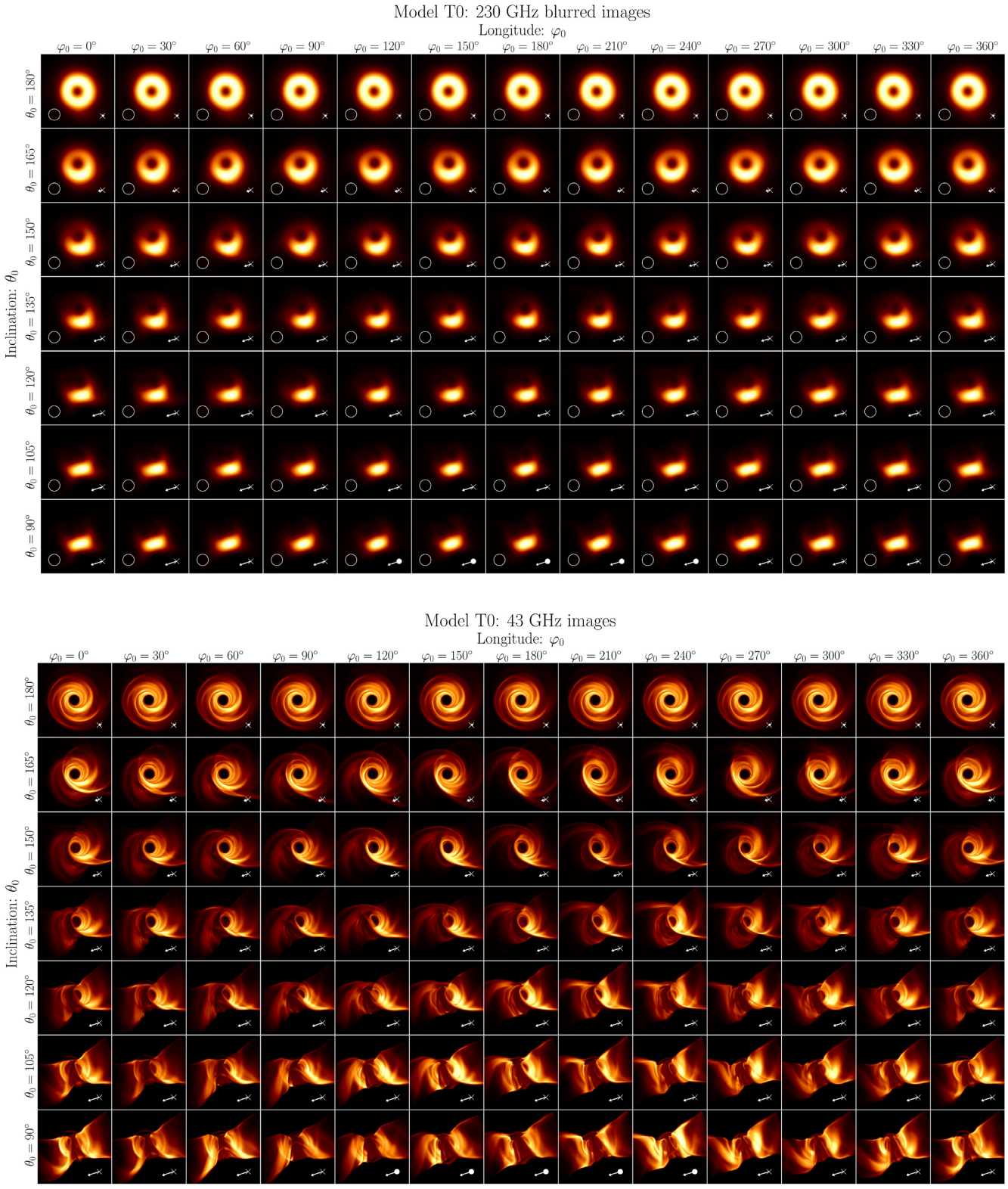

Figure C1. Single snapshot images at 230 and 43 GHz scaled to M87 and rotated to fit the M87 jet PA for different values of the observer inclination θ_0 and longitude φ_0, for aligned model `T0` with $R_{\rm h} = 10$. The box sizes are 110×110 and 150×150 μas^2 for the 230 and the 43 GHz images, respectively. The white arrow indicates the BH spin vector direction with the arrow length illustrating the spin projection on to the image plane. The X (O) indicates whether the BH spin vector is pointing into (out of) the image plane. These images are similar to the ones considered in EHTC (2019b), where GRMHD models were used to interpret the M87 image. Refer to Section 4.3 for further details.

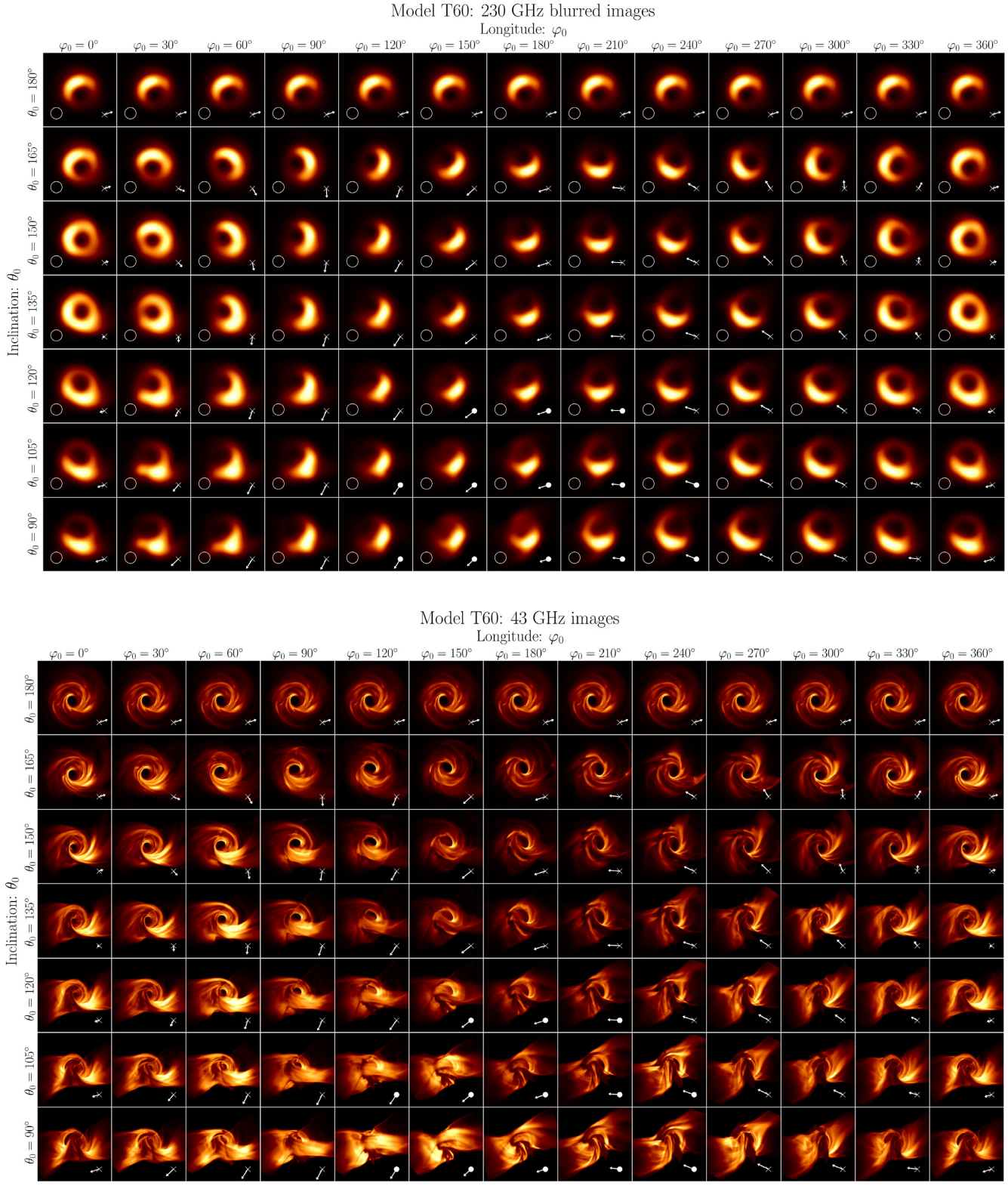

Figure C2. Single snapshot images at 230 and 43 GHz scaled to M87 and rotated to fit the M87 jet PA for different values of the observer inclination θ_0 and longitude φ_0, for tilted model `T60` with $R_{\rm h} = 10$. The box sizes are 110×110 and 150×150 μas^2 for the 230 and the 43 GHz images, respectively. The arrow direction and length indicates the BH spin direction and projection on to the image plane, with X (O) meaning into (out of) the plane. The warping of the disc and jet significantly alter the 43 GHz images.

This paper has been typeset from a TEX/LATEX file prepared by the author.